Modelling and numerical simulations of heat and mass transfer in multiphase flow during the release of liquid ammonia from a storage tank through the piping system to the open atmosphere

Vladimir Molkov, Srinivas Sivaraman, Donatella Cirrone, Benjamin Truchot, Dmitriy Makarov

▶ **To cite this version:**

Vladimir Molkov, Srinivas Sivaraman, Donatella Cirrone, Benjamin Truchot, Dmitriy Makarov. Modelling and numerical simulations of heat and mass transfer in multiphase flow during the release of liquid ammonia from a storage tank through the piping system to the open atmosphere. International Journal of Heat and Mass Transfer, 2025, 246, pp.127097. ⟨10.1016/j.ijheatmasstransfer.2025.127097⟩. ⟨hal-05065253⟩

HAL Id: hal-05065253

https://hal.science/hal-05065253v1

Submitted on 13 May 2025

HAL is a multi-disciplinary open access archive for the deposit and dissemination of scientific research documents, whether they are published or not. The documents may come from teaching and research institutions in France or abroad, or from public or private research centers.

L'archive ouverte pluridisciplinaire **HAL**, est destinée au dépôt et à la diffusion de documents scientifiques de niveau recherche, publiés ou non, émanant des établissements d'enseignement et de recherche français ou étrangers, des laboratoires publics ou privés.

Distributed under a Creative Commons CC BY-NC-ND 4.0 - Attribution - Non-commercial use - No Derivative Works - International License

International Journal of Heat and Mass Transfer 246 (2025) 127097

Contents lists available at ScienceDirect

International Journal of Heat and Mass Transfer

journal homepage: www.elsevier.com/locate/ijhmt

Modelling and numerical simulations of heat and mass transfer in multiphase flow during the release of liquid ammonia from a storage tank through the piping system to the open atmosphere

Vladimir Molkov [a], Srinivas Sivaraman [a,*], Donatella Cirrone [a], Benjamin Truchot [b], Dmitriy Makarov [a]

[a] HySAFER Centre, Ulster University, Newtownabbey BT37 0QB, United Kingdom
[b] INERIS - Institut National de l'Environnement Industriel et des Risques, France

ARTICLE INFO

Keywords:
Ammonia
Storage tank
Multiphase flow
Phase transition
Heat and mass transfer
Release to the atmosphere
CFD model
Validation

ABSTRACT

The aim of this study is to develop a contemporary CFD model of the multiphase flow of ammonia from a bulk liquid part of the storage vessel through the release piping to the atmosphere. The model is validated against the experiment with a 12 m^3 tank pressurised to 0.5357 MPa(g), i.e. Test No.4 of 560 s duration conducted by INERIS with release from the liquid bulk. The volume-of-fluid (VOF) method is applied for shared velocity and temperature of liquid and vapour phases of ammonia. The heat and mass transfer between liquid and vapour is simulated by modified Lee's evaporation-condensation model, accounting for the heat transfer from/to equipment and environment. A unique feature of the model is the phase change mechanism with varying mass transfer rates based on the transient volume fractions of liquid and vapour in a multiphase flow. This allowed to account for computationally unaffordable simulations of changing in time contact surface area between dispersed liquid and gaseous phases and avoid associated numerical complications. The model effectively captures the complex heat and mass transfer phenomena, including the cooling effect of evaporation in the piping and at the nozzle. The value of the time relaxation parameter and a multiplier accounting for the increase of contact surface between liquid and vapour in the pipe flow are defined by the inverse problem method through the comparison of simulations with the experiment. Simulations accurately reproduced experimental pressure and temperature dynamics in the storage tank, piping system and nozzle, and the total released mass of ammonia of 2352 kg.

1. Introduction

Ammonia is a hydrogen carrier with exceptional potential for driving the decarbonisation of the maritime sector. This is owing to its properties encompassing a high energy density and substantially superior hydrogen density in both volumetric and gravimetric terms when compared to other carriers [1,2]. Ammonia is typically stored and transported under elevated pressure at ambient temperature conditions. The structural integrity of liquid ammonia storage tanks and piping systems may be compromised due to surface imperfections, fatigue, and corrosion. These factors can cause significant deterioration, resulting in a hole/crack formation in either ullage or liquid phase space, potentially leading to the failure of a pressurised vessel and the release of toxic and flammable ammonia. In such incidents, the stored ammonia undergoes a transition to a non-equilibrium state, becoming superheated due to pressure drop and consequently giving rise to a two-phase flow with flash evaporation. Jet release into the atmosphere can result in serious safety implications. This type of incident with the release of toxic and flammable substances can lead to catastrophic consequences in terms of loss of human lives, property and environmental damages. The same heat and mass transfer phenomena are characteristic of ammonia bunkering/debunkering or controlled release from a storage tank through a release piping to the atmosphere.

The thermal non-equilibrium-driven flashing phenomenon is classified into either static or dynamic flashing, depending on the mode of release or leakage location [3]. The release of the gaseous phase from the ullage space of a storage system initiates static flashing within the stored liquid medium [3]. Previous studies were focused on understanding the transient behaviour of pressurised and/or cryogenic liquids under static flashing conditions caused by vapour outflow from the ullage space of a storage system. The pressure recovery phenomenon during the initial

* Corresponding author.
E-mail address: sivaraman-s@ulster.ac.uk (S. Sivaraman).

https://doi.org/10.1016/j.ijheatmasstransfer.2025.127097
Received 6 January 2025; Received in revised form 13 March 2025; Accepted 6 April 2025
Available online 14 April 2025
0017-9310/© 2025 The Author(s). Published by Elsevier Ltd. This is an open access article under the CC BY-NC-ND license (http://creativecommons.org/licenses/by-nc-nd/4.0/).

Nomenclature

Abbreviations

AV	*Automatic valve*
L/D	*Length-to-Diameter ratio*
MV	*Manual valve*

Latin

C	*Speed-of-sound (m/s)*
c_p	*Specific heat capacity at constant pressure* $(J/kg/K)$
c_v	*Specific heat capacity at constant volume* $(J/kg/K)$
d	*Shortest distance to the near wall (m)*
D	*Diffusion coefficient* (m^2/s)
g	*Gravity acceleration* (m/s^2)
h	*Enthalpy* (J/kg)
I	*Unit tensor (-)*
$\vec{J}$	*Diffusion flux* $(kg/m^2/s)$
k	*Thermal conductivity* $(W/m/K)$
k_E	*Turbulent kinetic energy (m2/s2)*
K	*von Karman constant (-)*
L_H	*Latent heat of evaporation-condensation (J/kg)*
M_{air}	*Molecular mass of air (kg/kmol)*
M_{gNH3}	*Molecular mass of ammonia (kg/kmol)*
$\dot{m}_{lg}$	*Mass rate of evaporation* $(kg/s/m^3)$
$\dot{m}_{gl}$	*Mass rate of condensation* $(kg/s/m^3)$
$\dot{m}$	*Mass rate of phase transition* $(kg/s/m^3)$
P	*Pressure (Pa)*
Pr	*Prandtl number (-)*
R	*Universal gas constant,* $R = 8314\ J/kmol/K$
r	*Time relaxation parameter (1/s)*
r_f	*Model multiplier (-)*
S	*Strain rate magnitude (1/s)*
S_{ij}	*Mean rate of strain tensor (1/s)*
Sc	*Schmidt number (-)*
S_E	*Source term in the energy equation* $(J/s/m^3)$
T	*Temperature (K)*
T_{sat}	*Saturation temperature (K)*
V	*Specific volume of mixture* (m^3/kg)
$\vec{v}$	*Velocity (m/s)*
v_y	*Velocity at a specific height (m/s)*
x	*Mixture quality (-)*
y	*Vertical height coordinate (m)*
y_0	*Ground roughness characteristic*
Y_{air}	*Air species mass fraction (-)*
Y_{gNH3}	*Ammonia vapour species mass fraction (-)*

Greeks

α	*Volume fraction (-)*
γ	*Ratio of specific heats (-)*
μ	*Dynamic molecular viscosity* $(kg/m/s)$
ρ	*Density* (kg/m^3)
σ	*Surface tension coefficient (N/m)*
ω	*Turbulent dissipation rate (1/s)*

Subscripts

air	*Air*
g	*Gaseous phase*
l	*Liquid phase*
gNH_3	Ammonia *vapour*
sat	*Saturation*
turb	*Turbulent*

Superscripts

T	*Tensor*
UU	*Ulster University*

stage of a tank depressurisation by vapour outflow was analysed for different substances, including liquid nitrogen [4–6], water [7–9], refrigerants [10], liquid hydrogen [11,12], and recently, liquid ammonia by the authors of this study [13]. The flash boiling of ammonia and associated pressure recovery phenomenon during venting from the ullage space is studied and described in detail in our work [13]. Here we are focusing on the release from the bulk liquid ammonia area of the storage tank.

The release from the liquid phase of the storage system triggers dynamic flashing [3]. The phase change in the dynamic flashing scenario mainly occurs within the discharging jet from the container or a piping system due to a significant pressure drop. This results in superheated conditions for liquid, its primary breakup during evaporation, subsequent secondary breakup, and formation of a two-phase flow with a dispersed mixture of liquid droplets and vapour [14]. The flashing of liquid occurs either in the piping system, i.e. internal flashing, or in the atmosphere outside the exit nozzle, i.e. external flashing [15].

Previous studies have notably placed significant focus on the unintended release of superheated liquids rapidly transforming into flashing jets when released into the atmosphere [16]. The primary emphasis of these studies has centred on understanding the flow dynamics during release and the downstream behaviour of released substances in the atmosphere. These studies aimed to develop risk assessment guidelines related to the toxicity and flammability of flashing releases. However, it remains imperative for reliable assessment of hazards and associated risks, not only to simulate the dispersion of flashing release out of the nozzle but to understand the upstream and in the nozzle behaviour of the tank-piping-atmosphere system defined by the heat and mass transfer as it apparently affects the hazard distances. Understanding pressure and temperature dynamics in the system under depressurisation is important to formulate protocols for safer management of storage tanks in ammonia infrastructure, including bunkering terminals and hydrogen refuelling stations.

In 2013, DNV and TNO [17] carried out a collaborative experimental investigation of the dynamics of the two-phase release of pressurised liquid CO_2 from a storage vessel. The setup featured a 500 L stainless steel pressure vessel with 30 mm wall thickness, initiating release oriented horizontally at a height of 188 cm and the release valve axis positioned 100 mm above the tank bottom. Trials were conducted at ambient conditions of 20 °C and 65 % relative humidity, examining initial pressures of 8.5 MPa(g), 11.8 MPa(g), and 14.8 MPa(g). Terminating outflow at pressures 1.0 to 1.5 MPa(g) prevented ice formation at the outlet nozzle and vessel. Pressure decay within the tank transitioned rapidly from an initial sub-cooled phase to a quasi-steady saturated state before accelerating towards the end of release as the tank content became purely vapour [17] The authors indicated that no solid CO2 was formed at the nozzle or in the vessel during trials, and any potential solid CO_2 formed downstream of the nozzle immediately undergoing sublimation.

In 2019, Zhu et al. [18] experimentally investigated the two-phase release of superheated water, emphasising internal system dynamics during the tank depressurisation. They used a 20 L insulated tank to initiate the release. The effect of different factors, including storage pressure, liquid superheat, and nozzle diameter, on the flashing release was analysed. The tests were performed at storage pressures 0.6 MPa(g), 1.1 MPa(g), and 1.6 MPa(g), in the range of liquid superheat between 20 °C and 40 °C, and nozzle diameters of 2 mm, 3 mm, and 4 mm. The conclusion was that the increase in storage pressure, liquid superheat,

and nozzle diameter resulted in the increased mass flow rate of the flashing jet. The liquid superheat had the predominant impact on the pressure decay characteristics in the storage tank. For example, nearly 48 % higher pressure during the quasi-steady flashing release period was observed when the liquid superheat was raised from 20 °C to 40 °C. This is attributed to the growth in evaporation rate in the tank with the increase of liquid superheat.

In 2021, Guo et al. [19] performed an experimental study to investigate the leakage and the flashing release of refrigerant R134a (tetrafluoroethene) from a pressurised vessel. The vessel volume was 2 L with an operating temperature range from −20 °C to 200 °C. The storage tank, prior to release, contained 1 kg of liquid R134a at a pressure of 0.72 MPa(g). The release was terminated when the pressures dropped to 0.01 MPa(g). The study aimed to analyse the impact of release nozzle diameters and length-to-diameter (L/D) ratio on superheated liquid release. Nozzle diameters ranged from 0.8 mm to 3 mm, with corresponding L/D varying from 1.33 to 5.00. Experiments took place under ambient conditions of 30 °C and 70 % humidity. The tank depressurisation rate increases as the L/D decreases and the temperature reduction rate in the tank increases with increasing L/D. Initially, a 1 °C temperature rise was observed due to thermal stratification in liquid R134a, followed by rapid temperature decrease as the liquid level dropped below the thermal probe during the release process.

Understanding heat and mass transfer during two-phase flashing releases of ammonia, along with the dynamic responses of a multiphase flow in the system tank-piping-atmosphere to depressurisation, is of paramount importance for safety provisions of ammonia storage and use. These insights are instrumental in defining scientifically based hazard distances defined by toxicity or flammability limits. The lack of computational models hampers understanding heat and mass transfer processes and the associated safety parameters, including hazard distances, during incidental loss-of-containment or scheduled debunkering and maintenance operations. In this context, having access to validated, contemporary models is crucial for advancing inherently safer tank management practices, especially with the increasing use of ammonia as a hydrogen carrier and marine fuel. Validated CFD models are critical for assessing hazards, incident consequences and risk management, safety engineering and defining safety protocols for emerging green energy infrastructure [20–22].

To the best of the authors' knowledge, no research has been performed and published to comprehend the details of heat and mass transfer during the flashing release of liquid ammonia from a pressurised storage tank through a piping system to the atmosphere. This study aims to close this knowledge gap by developing and validating a robust three-dimensional (3D) multiphase CFD model capable of predicting liquid ammonia's dynamic flash boiling behaviour during tank depressurisation. The paper describes a modified method for the simulation of the liquid-vapour phase transition to accurately model the evaporation-condensation of ammonia in the storage vessel, in the release piping system, including the nozzle, and in the atmosphere.

2. Validation experiment

Numerical simulations of the dynamic flash boiling of ammonia in the tank, piping system that includes the nozzle and the atmosphere using a developed multiphase CFD model were compared against Test No.4 from a series of large-scale field release of ammonia trials conducted by INERIS in the open atmosphere [23]. The experimental campaign comprised a total of 15 trial releases from either of three horizontally oriented cylindrical shape liquid ammonia storage tanks, each of 12 m^3 capacity. Only one of the three tanks was connected to the release system for each test. In 14 trials, liquid-phase ammonia was released, while one specifically addressed ammonia vapour venting from the ullage space of the storage tank. The double-walled tanks had 4.81 m external and 3.7 m internal length (thermal isolation of 0.5 m thickness; insulation material was set as polyurethane foam in this study), with an inner diameter of 1.874 m. A schematic of the experimental setup, including the release system details, is depicted in Fig. 1.

In Test No.4, liquid ammonia was released through the flexible hose, release system piping and the release nozzle to the open atmosphere using the automatic valve (AV). The manual valve (MV1) was installed on the storage tank and fully opened before the test. There was a flowmeter of 0.3 m in axial length and 41 mm internal diameter after MV1. The flowmeter was connected to the release system piping by a 10. 4 m long flexible hose with a 50.8 mm internal diameter. The release system piping comprises a 1.37 m long pipe of 50.8 mm internal diameter, equipped with a manual valve (MV2) and AV, a thermocouple (T6) and a pressure sensor (P2). The manual valves MV1 and MV2 have a smaller compared to hose and piping internal diameter of 38.1 mm while the AV is a full section valve with a 50.8 mm internal diameter. The release system is connected to a release nozzle of 0.19 m in length and 50.8 mm internal diameter. Thermocouple T7 is in the centre of the release nozzle, and pressure sensor P3 is placed 11 cm before the nozzle exit. The release system and the nozzle were oriented horizontally at 1.015 m above the ground.

The initial pressure in the tank (P1) and the connected piping (P2) prior to the beginning of release was 0.5357 MPa(g). The initial temperature at sensor T6 located 0.49 m before MV2 was 15.19 °C, which does not correspond to the saturated conditions of liquid ammonia for the initial pressure measured at P2 (saturation temperature for pressure 0.5357 MPa(g) is 11.05 °C). Thus, it can be concluded that ammonia vapour at higher temperatures was present in the release system before the AV prior to its opening.

Fig. 2 shows the location of five thermocouples (T1-T5) in the storage tank to monitor the ammonia temperature change during the release. The thermocouples are located at the following heights from the bottom of the tank: T1 at 1.45 m, T2 - 1.1 m, T3 - 0.75 m, T4 - 0.4 m, and T5 - 0.05 m. As depicted in Fig. 2, the thermocouples showed thermal stratification in the ammonia storage tank before the release.

The initial level of liquid ammonia was not experimentally recorded and estimated in this study as 1.24 m from the tank bottom. Thermocouple T1-T5 located within the tank revealed that the temperature at location T1 was 9.87 °C at the time of the AV opening. This is higher than temperatures recorded by T2-T5 and indicates the presence of ammonia vapour at a height of 1.45 m from the tank bottom. Thus, the initial liquid ammonia level was estimated to be between the thermocouples T1 and T2, i.e. at a height between 1.10 m and 1.45 m from the tank bottom. Given this data uncertainty, the authors assumed an initial liquid level of 1.24 m from the tank bottom, which corresponds to a 70 % fill level. The thermal stratification of ammonia vapour in the ullage space measured at T2 and T1 was extrapolated till the tank top in this study, as shown in Fig. 2.

In Test No.4, the experimentalists remotely operated the AV to trigger the release from the storage tank (both manual valves MV1 and MV2 were fully open). The AV was closed at 560 s to stop the release. Subsequently, after 560 s, the pressures monitored by sensors P2 and P3 returned to their expected values (P2 to the pressure in the tank and P3 to the atmospheric pressure), indicating the AV closure time. Due to issues with the flowmeter, only the average mass flow rate was reported based on the total mass released, which was measured as 2352 kg.

3. The CFD model

3.1. Governing equations for multiphase flow

The developed 3D CFD model of multiphase flow was employed to solve mass, momentum, energy, and species transport conservation equations. The study applied the Volume-of-Fluid (VOF) multiphase model to simulate heat and mass transfer processes during flash boiling of ammonia resulting from the pressure drop in the system tank-piping-atmosphere after the start of depressurisation. The flow turbulence is simulated by the RANS SST k-ω model following Fluent's

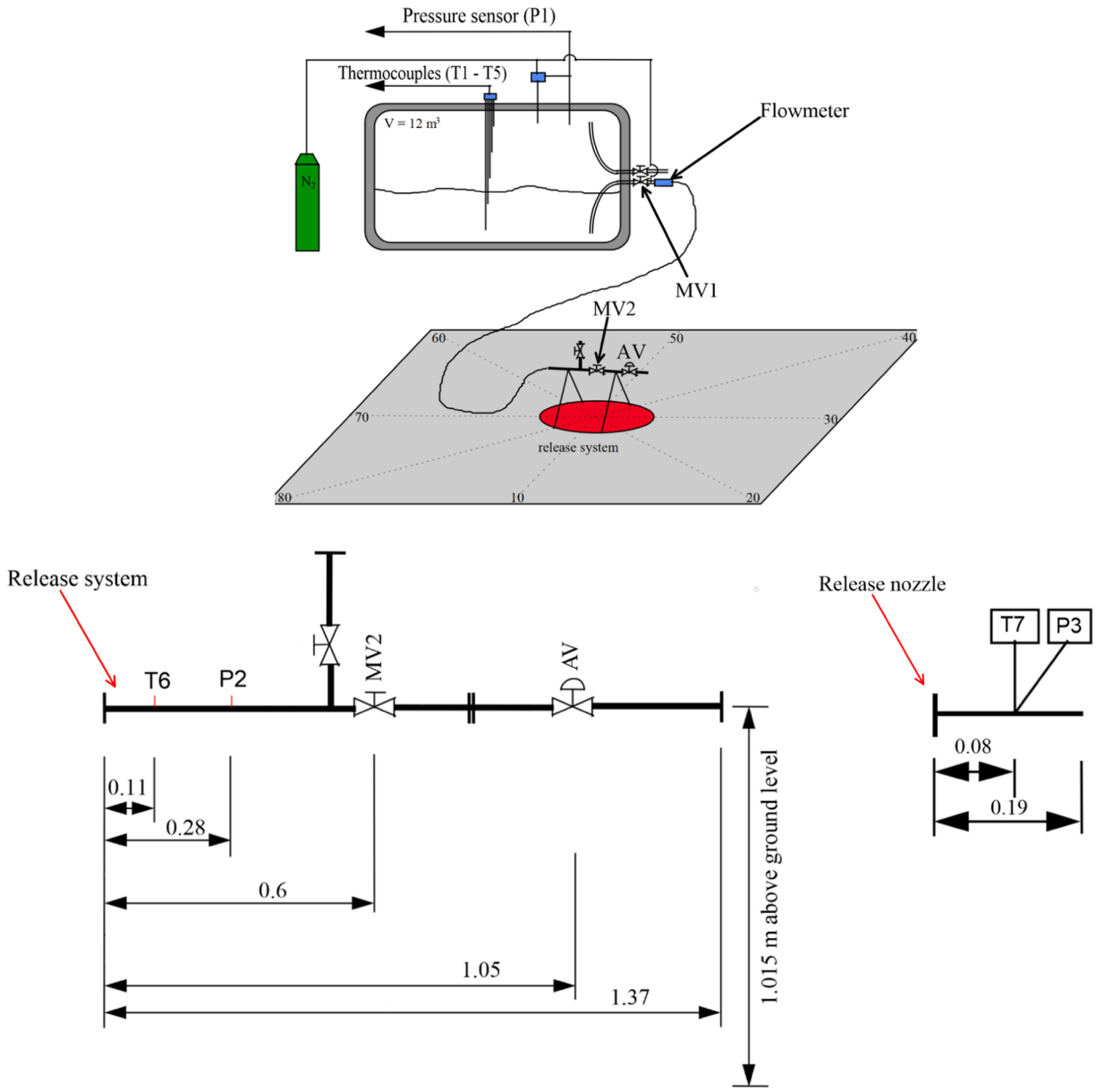

Fig. 1. Schematic of the experimental setup (top), the release system piping (bottom left) and the release nozzle (bottom right), including locations of pressure (P) and temperature (T) sensors [23]. Note: all distances are in meters.

recommendation, as it enables essential turbulence damping required to capture interfacial instabilities in numerical simulations of flash boiling flows [24].

3.1.1. The VOF model

Numerical simulations of multiphase flow for fluid-fluid systems in this work utilise the Euler-Euler approach. This study employs the VOF model based on the homogeneous equilibrium model (HEM). The HEM approach treats phases as interpenetrating continuums, sharing temperature and velocity fields. The VOF model is a preferred practical choice offering effective liquid/gas interface tracking in flash boiling flows [12,13,25–27] while maintaining computational efficiency. Other multiphase models, such as the mixture multiphase model [28], allow for velocity slip between phases while having same temperature fields between phases. In contrast, the most comprehensive and resource-demanding approach is the non-homogeneous non-equilibrium multiphase modelling (NHNEM) that allows to separate temperature and velocity fields for each of the phases [29].

The VOF model adheres to the concept of phasic volume fraction, α, where the volume of one phase, e.g. gaseous, is mutually exclusive with another, i.e. liquid, ensuring that the sum of volume fractions in a control volume (CV) equals unity, i.e. $\alpha_g + \alpha_l = 1$.

In multiphase flows, the interaction between gas and liquid phases can vary depending on several factors. In typical laminar or stratified flows, which is representative of low Reynolds and Weber numbers, surface tension and viscous forces dominate the flow, thus resulting in a stable distinct interface between the phases. In contrast, in the case of flows with high Reynolds and Weber numbers, the inertial forces and turbulence overcome the surface tension and viscous forces, leading to the breakup of the interface and creating dispersed flow patterns, with droplets ripped off from the bulk liquid and bubbles forming throughout the flow. This behaviour is especially prominent in flashing flows through pipes, where rapid vaporisation and gas-phase acceleration lead to increased turbulence, causing the liquid phase to fragment into fine droplets. This results in dispersed or mist-flow regimes. To account for this behaviour in the CFD model, the authors incorporated the

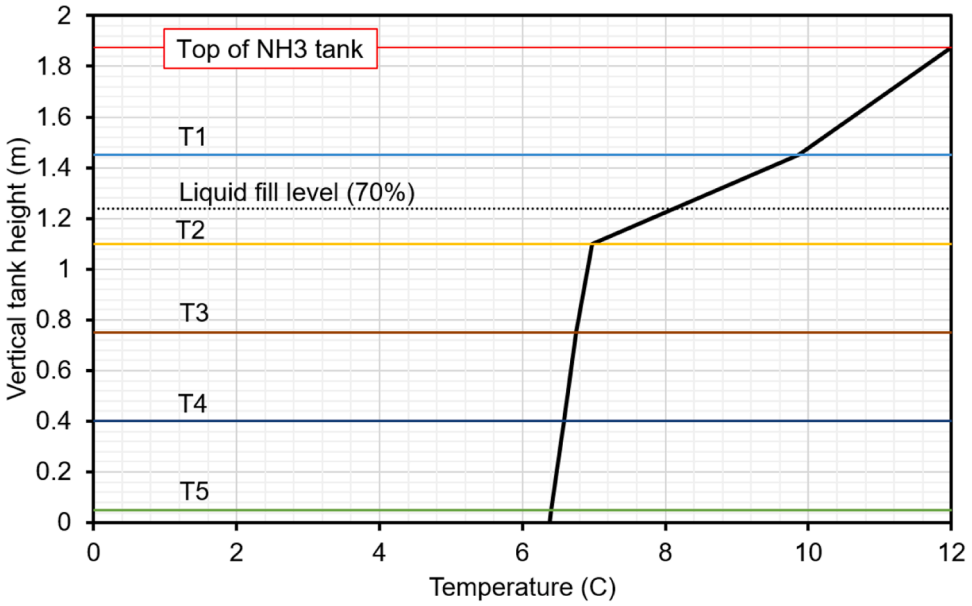

Fig. 2. Thermal stratification in the ammonia storage tank digitised from the experimental data.

"dispersed" interface modelling option in Fluent, ensuring a realistic representation of the phase interactions during flash boiling [24].

In this study, the liquid phase represents liquid ammonia, while the gaseous phase is a mixture of ammonia vapour and air. The model considers the gaseous phase mixture as the primary phase and the liquid ammonia phase as the secondary phase in the numerical formulation. The volume fraction equation is solved for the secondary phase:

$$\frac{\partial}{\partial t}(\alpha_l \rho_l) + \nabla\left(\alpha_l \rho_l \vec{v}_l\right) = S_{\dot{m}}, \tag{1}$$

where $S_{\dot{m}}$ is the source term of mass transfer between gaseous and liquid phases. The source term for interphase mass transfer, $S_{\dot{m}}$, represents the net mass transferred during evaporation or condensation. In physical reality, evaporation and condensation can occur simultaneously within the same volume of space. However, in numerical models, a control volume can typically exhibit either evaporation or condensation at a given time step, not both. Further elaboration on the mass transfer source term is provided in the "Phase change mechanism" section below. While the liquid phase volume fraction is calculated from Eq. (1), the primary gas phase volume fraction is calculated following the constraint: $\alpha_g + \alpha_l = 1$.

The study addresses the species transport by solving the following equation for ammonia vapour species (gNH_3) within the gas-phase mixture:

$$\frac{\partial}{\partial t}\left(\alpha_g \rho_g Y_{gNH_3}\right) + \nabla\cdot\left(\alpha_g \rho_g \vec{v}_g Y_{gNH_3}\right) = \nabla\cdot\left[\alpha_g\left(\rho_g D + \frac{\mu_{turb}}{Sc_t}\right)\nabla Y_{gNH_3}\right] + \dot{m}_{gl} - \dot{m}_{lg}, \tag{2}$$

and the mass fraction of air is then derived from the equation:

$$Y_{air} = 1 - Y_{gNH_3}. \tag{3}$$

The model computes phasic attributes of liquid and gaseous phases, such as phase densities and viscosities, by utilising individual volume fractions derived from conservation equations using the following equations, respectively [24]:

$$\rho = \alpha_l \rho_l + (1 - \alpha_l)\rho_g, \tag{4}$$

$$\mu = \alpha_l \mu_l + (1 - \alpha_l)\mu_g. \tag{5}$$

The phases share a single momentum conservation equation, thus resulting in a single velocity field. The momentum equation accounts for all phases through their respective properties, such as density and viscosity:

$$\frac{\partial}{\partial t}(\rho \vec{v}) + \nabla\cdot(\rho \vec{v}\vec{v}) = -\nabla P + \nabla\cdot\left((\mu+\mu_{turb})\left(\nabla\vec{v} + \nabla\vec{v}^T\right) - \frac{2}{3}(\mu+\mu_{turb})(\nabla\cdot\vec{v})I\right) + \rho\vec{g}. \tag{6}$$

The turbulent viscosity (μ_{turb}) is calculated following the formulation of the SST k-ω turbulence model [24]:

$$\mu_{turb} = \frac{\rho k_E}{\omega}\left(\frac{1}{\max\left[\frac{1}{C^*}, \frac{SF_2}{0.31\omega}\right]}\right), \tag{7}$$

$$F_2 = \tanh\left(\max\left[2\frac{\sqrt{k_E}}{0.09\omega d}, \frac{500\mu}{\rho d^2 \omega}\right]\right), \tag{8}$$

where C^* is the variable that is calculated as a function of turbulent kinetic energy, k_E, dissipation rate, ω, and viscosity, μ; F_2 is known as the blending function responsible for the transition between the near-wall and free-stream conditions and $S = \left(2S_{ij}S_{ij}\right)^{1/2}$ is the strain rate magnitude.

The density of the gaseous phase, composed of ammonia vapour and

Table 1
Models of interfacial mass transfer: the original Lee's model [31] and the modified Ulster University (UU) model developed in this study.

Mass transfer model	Model equations
Original Lee's model [31]	$\dot{m}_{lg} = \frac{r\ \alpha_l\ \rho_l\ (T_l - T_{sat})}{T_{sat}}$ if $T_l > T_{sat}$(evaporation), (15a)
	$\dot{m}_{gl} = \frac{r\ \alpha_g\ \rho_g\ (T_{sat} - T_g)}{T_{sat}}$ if $T_{sat} > T_g$(condensation). (15b)
Modified model, this study	$\dot{m}_{lg}^{UU} = \frac{r_f \cdot r\alpha_l\rho_l(T_l - T_{sat})}{T_{sat}}$ if$T_l > T_{sat}$(evaporation), (16a)
	$\dot{m}_{gl}^{UU} = \frac{r_f \cdot r\alpha_g\rho_g(T_{sat} - T_g)}{T_{sat}}$ if$T_{sat} > T_g$(condensation). (16b)

air, is computed using equations of state:

$$\rho_g = \frac{P}{RT\left(\frac{Y_{air}}{M_{air}} + \frac{Y_{gNH3}}{M_{gNH3}}\right)}. \quad (9)$$

The energy equation is also shared between the gas and liquid phases [24]:

$$\frac{\partial}{\partial t}(\rho E) + \nabla\cdot(\vec{v}[\rho E + P]) = \nabla\cdot\left[(k + k_{turb})\nabla T + h_g\left(\rho_g D + \frac{\mu_{turb}}{Sc_{turb}}\right)\nabla Y_{gNH3} + \vec{v}\,(\mu + \mu_{turb})\left(\left(\nabla\vec{v} + \nabla\vec{v}^{T}\right) - \frac{2}{3}(\nabla\cdot\vec{v})I\right)\right] + S_E, \quad (10)$$

$$k_{turb} = \frac{C_p\mu_{turb}}{Pr_{turb}}. \quad (11)$$

here k_{turb} represents the turbulent thermal conductivity with turbulent Prandtl number Pr_{turb}=0.85. The total energy, E, and temperature, T, are calculated as mass-averaged variables. The equation for the total energy is:

$$E = \frac{\alpha_g\rho_g E_g + \alpha_l\rho_l E_l}{\alpha_g\rho_g + \alpha_l\rho_l}. \quad (12)$$

where, $E_l = h_l - \frac{P}{\rho_l} + \frac{\vec{v}^2}{2}$ is the energy source contribution of the liquid phase (internal energy plus kinetic energy) and $E_g = h_g - \frac{P}{\rho_g} + \frac{\vec{v}^2}{2}$ is the energy source contribution of the vapour phase.

The source term S_E in the energy equation represents the volumetric heat source/sink, encompassing heat release from condensation or heat absorption during evaporation. It functions as either a heat source or a heat sink, depending on the dominant phase change process within each CV. It is calculated explicitly as:

$$S_E = S_{\dot{m}}\, L_H, \quad (13)$$

where $S_{\dot{m}} = \dot{m}_{gl} - \dot{m}_{lg}$ is the net mass transfer rate due to phase change and L_H is the latent heat of evaporation/condensation. The latent heat of evaporation/condensation is derived based on the NIST database [30] and is expressed as a function of temperature for saturated conditions of ammonia vapour and liquid valid for the range of temperatures 239.00–293.15 K:

$$L_H\ (J/kg) = -9.7557\cdot T^2 + 1771.9\cdot T + 2000000. \quad (14)$$

3.1.2. Phase change mechanism

The phase change is simulated here using Lee's evaporation/condensation model as the basis. The Lee's model is a mechanistic framework developed in 1980 [31] that initiates phase transitions between liquid and gas phases in response to thermal and pressure variations. According to this model, evaporation occurs when the liquid temperature (changes inertially compared to the pressure change) exceeds the saturation temperature, i.e. the boiling temperature unambiguously defined by the transient pressure, and condensation occurs when the gas phase temperature drops below the saturation temperature. In the scenario investigated in this study, the dynamic flashing phenomenon is induced by the pressure drop in the piping system and then in the atmosphere during the release of liquid ammonia from the tank at initial saturation conditions. The pressure drop causes a decrease in the local saturation temperature, leading to phase change between liquid ammonia and its vapour, i.e. evaporation in such conditions. The original equations of Lee's model for the mass transfer source term are shown in Table 1, Eqs. (15a) and (15b), along with the modified in this work model, Eqs. (16a) and (16b), where the multiplier r_f accounts for the increase of interfacial surface area between flow in the tank and in the pipe:

Liquid and gas phase temperatures are shared within the control volume according to HEM modelling principles, i.e. $T_l = T_g$. The empirical coefficient "r", known as the *"time relaxation parameter"* [31], compensates for the intricate, fine-scale complexities influencing the problem-dependent liquid-gas interfacial mass and heat transfer not explicitly resolved or modelled in simulations. These include the interfacial surface area between liquid and gas, which defines the evaporation/condensation rate and depends on bubble/droplet diameter and bubble/droplet frequency, dynamics of bubble/droplet growth and collapse, etc. Thus, there can be no consensus on this empirical coefficient's "unique" value in numerical studies of different multiphase flow problems with boiling and condensation. The overview of previous research shows that the coefficient is calibrated for each specific experiment, resulting in a wide range of ten orders of magnitude difference values from 10^{-3} to 10^{7} [32–37]. In previous research by the authors on the pressure recovery phenomenon during rapid ammonia tank depressurisation by venting of the ullage space [13], the phase change rate in the bulk liquid ammonia was defined by the inverse problem method, i.e. by comparing simulation results with experimental data, using the Lee's model coefficient for the model calibration. The calibrated against the experimental data coefficient was found to be in the range r = 0.007–0.100, depending on the initial temperature of the stored liquid ammonia.

Although Lee's approach allows reasonable simulations of multiphase flow, it currently has two serious disadvantages: firstly, the empirical coefficient "r" is not known in advance and thus must be recalibrated for each experimental set-up, and, secondly, there is no knowledge of how it changes when flow conditions change drastically, e.g. when the flow of liquid from the quiescent bulk fluid in the tank changes to high-speed flow in the pipe. These difficulties reduce Lee's model's robustness as a predictive safety engineering tool. Hopefully, an increasing time collection of defined values of "r" for different problems would underpin a better understanding of its choice depending on a problem formulation, including problems with flow transition from a quiescent bulk fluid to flash boiling of high-speed two-phase flow in a pipe and the atmosphere.

In this study, the authors propose a modification to the existing interfacial mass rate change source term based on variations of flow conditions, enabling a more physical, i.e. apparent reduction of a real interfacial area with a volumetric fraction of either phase approaching zero. The modification makes the model numerically more robust, i.e. it excludes a sharp change of "r" in the calculation domain during calibration of the time relaxation parameter and associated numerical instabilities. The modified volumetric mass source term $\left(\dot{m}_{lg}^{UU} \text{and} \dot{m}_{gl}^{UU}\right)$ is defined by Eqs. (16a)-(16b) in Table 1. The original Lee's coefficient "r" is multiplied by an additional coefficient "r_f" that changes from 1 to its maximum value (to be defined by the inverse problem method), when the vapour phase fraction is increasing due to changing flow conditions, e.g. during flash boiling in a pipe due to pressure drop, and then "r_f" decreases from the maximum value back to 1 when the liquid phase fraction decreases tending to fully evaporate.

The interfacial area density plays a critical role in influencing the mass transfer rate between phases, with higher interfacial area density directly correlating to increased total area available for mass transfer

between phases. In the context of boiling processes in a release pipe, an increase in the volume fraction of vapour, α_g, at the beginning of the process of liquid from the tank entering a pipe, within the two-phase mixture leads to a higher interfacial area density and, consequently, an increased mass transfer rate between the phases. Various factors contribute to this phenomenon. At higher volume fraction of vapour, the flow changes to a mist or dispersed flow regime, where numerous droplets are formed due to physically existing shift velocity between the heavier (inertial) liquid phase and lighter gaseous phase in the pipe, which flows with higher velocity, creating turbulence and shear forces between liquid and gas. The increase of droplets' number with the simultaneous decrease of their diameter in a pipe flow from the storage tank provides a larger surface area-to-volume ratio compared to the case with fewer but larger droplets or bulk low-velocity liquid flow in the pipe. Consequently, a higher vapour volume fraction directly translates to more droplets in the flow, resulting in a greater contact surface area between the two phases. In high vapour volume fraction and real flow with velocity shift between phases, droplets rip off by gaseous flow from bulk liquid entering the pipe from the storage tank at Weber number above the critical value. Thus, the increase of interfacial area in the release pipe compared to the quasi-laminar flow of ammonia in the storage tank is a reason for the expected increase of "r" value in the release pipe, i.e. to the value of "$r_f \cdot r$" compared to the "r" value in the storage tank.

To incorporate the above-mentioned argumentation into the model and numerical simulations, the modification to the existing time relaxation parameter is proposed in this study by introducing a multiplier, "r_f", to the original time relaxation parameter "r". Building on the authors' previous research on flash boiling and the associated pressure recovery phenomenon [13], sensitivity analysis was conducted on the original time relaxation parameter "r" to refine the mass transfer rate within the storage tank. However, to accurately capture the complexities arising from the increased interfacial area density during intense boiling and multiphase flow in the piping system, which occurs during dynamic flashing, the correction factor, r_f, is introduced. This multiplier is applied specifically to the pipe and atmosphere regions to better represent the mass transfer dynamics under these conditions within the developed CFD model.

The multiplier, r_f, varies depending on the volumetric fraction of liquid and gaseous phases in the two-phase flow thus compensating by modelling the unresolved complexities associated with liquid/vapour interfacial area density change when either of the phases approaches zero. The varying parameter r_f is equal to 1 at liquid volume fraction equal to either $\alpha_l = 0$ ($\alpha_g = 1$) or $\alpha_l = 1$ ($\alpha_g = 0$).

By the inverse problem method, the authors investigated the influence of the original time relaxation parameter "r" and different parametric dependencies introduced in this study for the first time r_f multiplier on volume fractions of liquid and gaseous ammonia. It was done to identify the most suitable multiplier function/profile and the maximum value attainable by the r_f multiplier at different limiting volume fractions of either of the phases involved in this study. The details and comparison of various r_f The section "CFD model calibration: time relaxation parameter and modified mass source term" provides multiplier profiles.

3.1.3. Computational domain and numerical details

A geometrically similar horizontal liquid ammonia tank and a connected piping release system were generated as parts of the computational domain to match the experimental set-up dimensions. The horizontal tank had an internal length of 3.7 m and an internal diameter of 1.874 m. The computational domain is extended from the equipment to the atmosphere with dimensions $L \times W \times H = 30\ m \times 20\ m \times 10$ m (see Fig. 3) with the release nozzle exit protruding 0.5 m into it. This part of the computational domain is important to ensure accurate flow conditions at the release nozzle exit (to exclude forcing it to be a boundary with continuously changing conditions), preventing disruption of flow behaviour and ammonia evaporation due to improper boundary conditions. The inlet boundary of the external domain behind the release nozzle is set as a velocity inlet for wind flow. The sides, top, and far-field boundaries are defined as pressure outlets at atmospheric pressure, i.e. 0 MPa(g) or 101,325 Pa(a). The dispersion of flashing ammonia release in the atmosphere is out of the scope of this study and will be reported in a follow-up paper.

The entire experimental setup including the tank, piping system, valves, pressure sensors, and thermocouples used to monitor the flow behaviour during ammonia release are shown in Fig. 4. The first manual valve MV1, with a 3/2-inch bore (38.1 mm), was positioned 0.55 m away from the internal tank surface, accounting for the 0.55 m insulation thickness (not included in the calculation domain and accounted for by the application of the shell conduction option of the software). The axis of MV1 and the connected piping system in the computational domain to release ammonia from the storage tank is set at 0.62 m from the bottom of the tank. After MV1 of 0.24 m of axial length, there was a flowmeter in the piping system, which was 0.3 m in axial length with 41 mm internal diameter as in the experiment. A 10.4 m flexible hose of an internal diameter of 50.8 mm connected the flowmeter to the release system. The release system of a 1.37 m long pipe with an internal diameter of 50.8 mm incorporated a second manual valve MV2 of 38.1 mm internal diameter and 0.24 m axial length, and a full-bore AV of 0.24 m length. Following the information from the experimentalists, all the

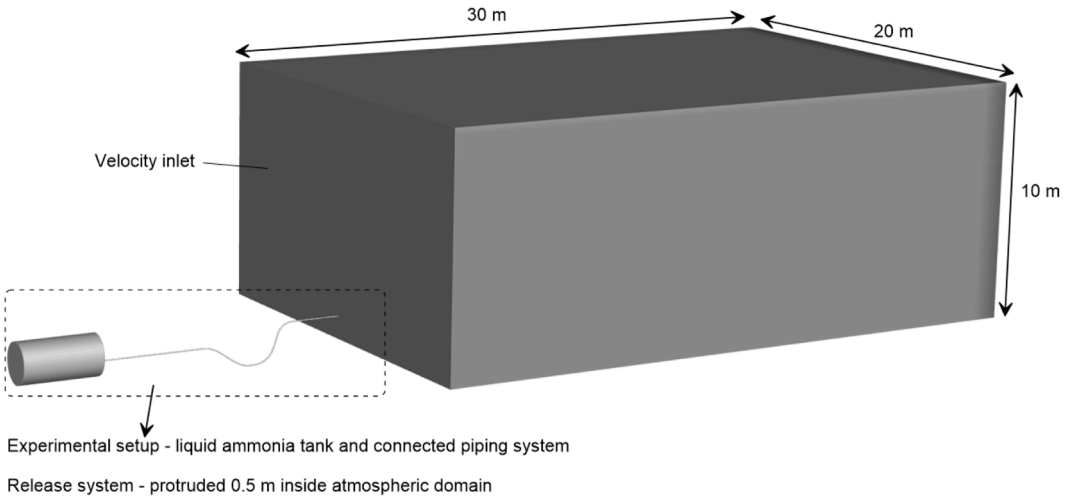

Fig. 3. Isometric view of the computational domain with the extended atmospheric area.

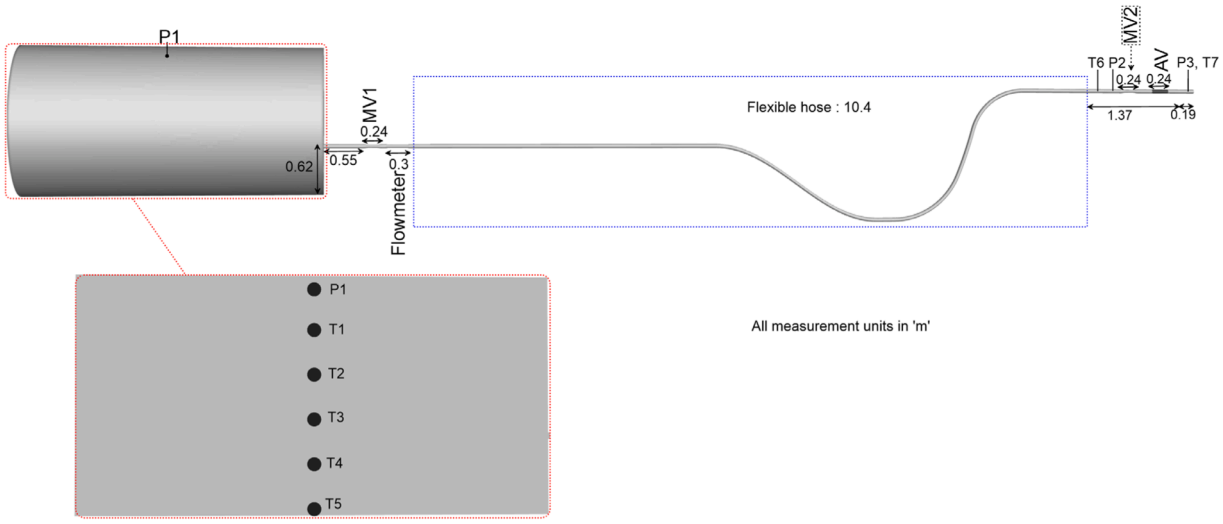

Fig. 4. Equipment part of the computational domain. Top: side view with pressure (P) and temperature (T) sensors. Bottom: zoomed-in central cross-section of the storage tank with sensors.

valves in the connected piping system were fully open, thus allowing flow through a 100 % cross-section of the respective internal diameters. The release system was subsequently linked to a 0.19 m long nozzle with the internal diameter of 50.8 mm.

Fig. 4 (bottom) provides a view of the central cross-section of the pressurised ammonia storage tank, indicating the positions of the pressure transducer and locations of thermocouples along the tank's height. Temperature measurements in the CFD model at respective thermocouple locations T1-T5 are monitored at the following distances from the tank's bottom surface: T1 - 1.45 m, T2 - 1.1 m, T3 - 0.75 m, T4 - 0.4 m, and T5 - 0.05 m. Thermocouples T6 and T7 are located at the axis of the pipe, respectively, at 1.441 m and 0.11 m from the exit surface of the nozzle before MV2 and after AV, respectively. Pressure sensor P1 is in the tank's ullage space, while sensors P2 and P3 are recorded at the centre of the pipe, respectively, at 1.28 m and 0.11 m from the nozzle exit surface. It is worth noting that temperature and pressure monitoring in the CFD model was performed at the exact locations reported in the experiment.

Fig. 5 demonstrates the numerical boundary mesh of the computational domain generated by ANSYS Meshing. The total number of hexahedral control volumes (CVs) in the domain is 317,260 with <20 % of the total CVs number present in the domain imitating the ambient atmosphere. In the extended domain, close to the orifice, a growth ratio of 1.1 was used, while a ratio of 1.2 was used farther from the orifice. The minimum orthogonal quality of the mesh was 0.51, with an average quality equal to 0.97 of possible 1.0. The grid sensitivity analysis is presented in the "Grid sensitivity analysis" section.

As described in the section "Validation experiment", the release piping system is filled with liquid ammonia in the flexible pipe and vapour ammonia at higher temperatures is present in the piping system close to the AV, which is evidenced by the initial readings at T6 thermocouple location. To incorporate in simulations the initial conditions like those observed experimentally, the numerical domain was initialised as shown in Fig. 6. The figure demonstrates the initialised liquid ammonia volume fraction in the flexible pipe (Fig. 6a), and the initial temperature in the domain (Fig. 6b). The flexible pipe was filled with liquid ammonia to the same height as the liquid height in the ammonia storage tank, being connected. After the experimental observations, the thermal stratification was initialised in the ammonia storage tank (see section "Validation Experiment" and Fig. 2).

The storage tank was initialised with liquid ammonia up to 1.24 m from the bottom, equivalent to a 70 % fill level. The ullage space in the tank was filled with ammonia vapour. The initial pressure in the storage tank and the release system till the initially closed AV is set equal to 0.5357 MPa(g) following the experimental readings of P1 and P2 sensors. The operating pressure in the release system close to the atmosphere, i.e. after the AV, and in the atmosphere is initialised as 0 MPa with the gauge pressure 101,325 Pa(g), i.e. atmospheric pressure 101,325 Pa(a) following P3 sensor readings. The initial temperature in the release system after the AV is set as 11.45 °C following experimental T7 readings (see Fig. 6b). The computational domain in the atmosphere is initialised with the temperature of 12.5 °C in accordance with the reported ambient temperature.

All solid wall surfaces, including ground, tank, piping system, flowmeter and valves, are treated as non-slip and non-permeable boundary surfaces. The ground is modelled as an adiabatic wall in this work focused on the flash boiling in the system, not dispersion in the atmosphere. The side faces, far-field faces, and the top face of the external

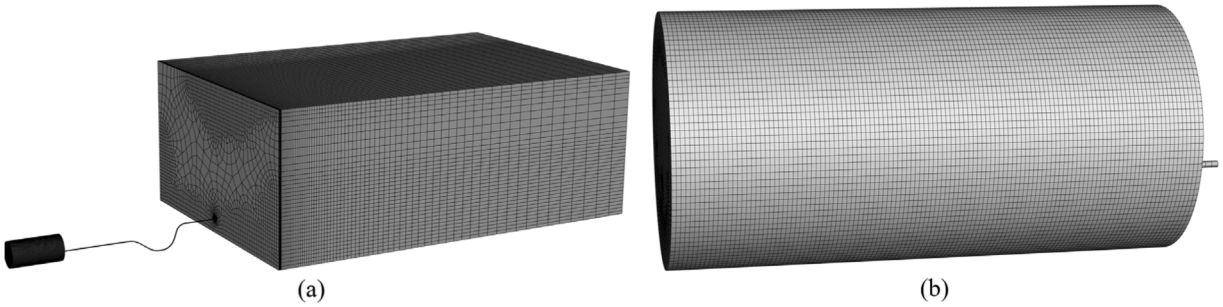

Fig. 5. (a) - boundary mesh of the total computational domain, (b) - zoomed-in boundary mesh of the ammonia storage tank.

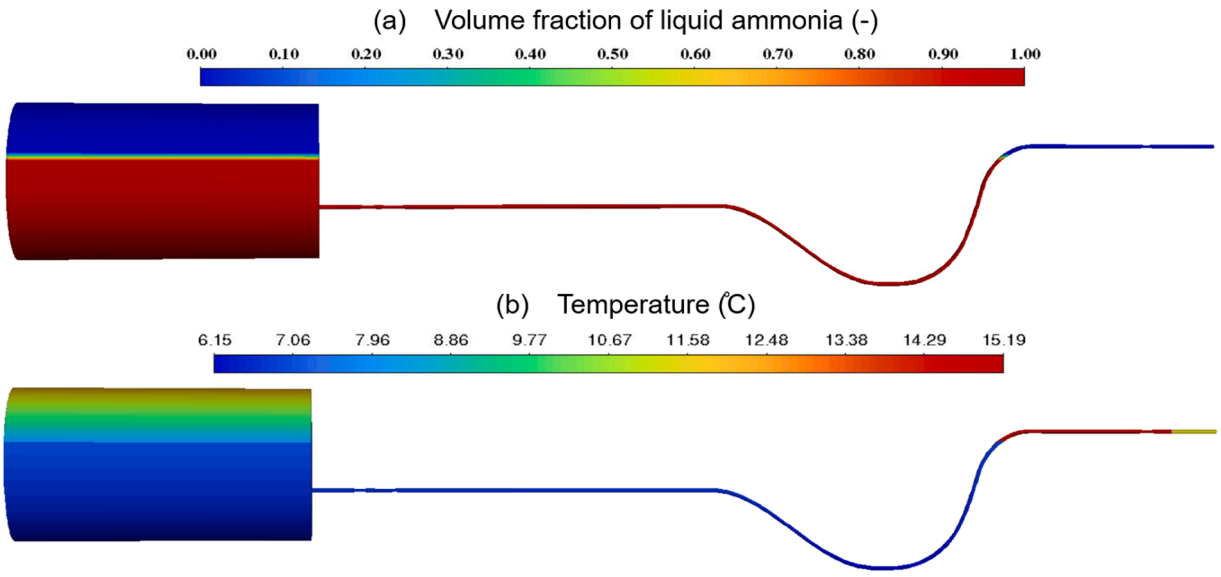

Fig. 6. Initial conditions in the equipment part of the computational domain: (a) - liquid ammonia volume fraction, (b) - temperature.

atmospheric domain are modelled as a pressure outlet boundary with pressure equal to 101,325 Pa(a). The inlet face of the external atmospheric domain behind the release nozzle is set as a velocity inlet, which is modelled with a wind profile following Eq. (17) conforming to the atmospheric boundary layer (ABL) theory [38,39]:

$$v_y = \frac{0.2944}{K}\cdot\ln(y/y_0). \quad (17)$$

Near the ground, wind flow velocity is lower and increases with height. The region where this friction influences wind speed is known as the ABL. To incorporate the ABL, this study applies the log-law profile from the Monin-Obukhov similarity theory, suitable for stable and unstable atmospheric conditions. In Eq. (17), v_y represents the wind velocity at a given height y, while K is the von Karman constant set at 0.4. The ground roughness characteristic, denoted as y_0, is assigned a value of 0.03 m. The constant coefficient value of '0.2944' is selected based on fitting the wind profile [39], ensuring that the wind velocity matches 4.12 m/s at a height of 7 m following the experimental meteorological data [23].

The rest of the equipment wall boundaries accounted for convective heat transfer with the atmosphere. The flexible pipe of 10.4 m in length is set as a rubber hose like in the authors' previous work [13]. The numerical domain presented only the internal wall of the double-walled storage tank, while the heat transfer between the inner wall and the insulation material was simulated using the "shell conduction option" of ANSYS Fluent following previously published studies [13,40]. The heat transfer between the outer tank wall and the atmosphere is accounted for by using the heat transfer coefficient of 7 W/m^2/K [41] with the ambient temperature of 12.5 °C. Following our previous work [13], in the shell conduction modelling, the first layer representing the tank's inner wall material, i.e. the wall in contact with ammonia, is assumed of 2 mm thick and made of carbon steel with thermal properties: c_p=484.6 J/kg/K, k = 51.0 W/m/K, ρ = 7849.8 kg/m^3. The second layer of shell conduction modelling representing the insulation material of the double-walled tank is set as polyurethane foam with a thickness of 550 mm and thermal properties as follows: c_p =1546.6 J/kg/K, k = 0.044 W/m/K, ρ = 192.0 kg/m^3.

The simulations are performed using ANSYS Fluent 2023R1 as the computational engine. Segregated pressure-based solver with SIMPLE-C pressure-velocity coupling is applied. Ammonia vapour density was calculated by the ideal gas equation of state (EoS) since the ammonia storage pressure in Test No.4, i.e. 0.5357 MPa(g), is significantly below the threshold of 4.9 MPa(g) that requires the use of real gas EoS for density calculations [42]. Liquid ammonia density is calculated as a function of temperature using the NIST database [30]. The material properties, including thermal conductivity, specific heat capacity and viscosity of liquid and vapour ammonia, are defined as a function of temperature using the NIST database [30] Table 2 presents the correlations of the physical properties of liquid and vapour ammonia. They are applicable in the temperature range 239.00–293.00 K.

The conservation equations are discretised using the first-order upwind numerical scheme to ensure numerical stability, and the diffusion terms are discretised using the second-order upwind numerical scheme. Time step advancement in the simulation was done by using a bounded second-order implicit numerical scheme.

4. Results and discussion

4.1. The grid independence analysis

Demonstrating grid independence is crucial to ensure the quality of the CFD model [43]. Three different grids of the same calculation domain are investigated for the initial phase of tank depressurisation and flash boiling of liquid ammonia during release from the storage tank through the piping system to the atmosphere.

It is important to note that, in the grid sensitivity study presented, the time relaxation parameter in the tank was set to $r = 0.007$, consistent with our previous work [13]. However, in the pipe, this value increases significantly by three orders of magnitude to $r_f \cdot r = 7.0$ due to the described model modifications suggested in this study (see section "Phase change mechanism"). This adjustment is based on the selected maximum value of the empirical coefficient increase by an additional

Table 2
Correlations for some of the physical properties of liquid and vapour ammonia.

Physical property	Correlation as function of temperature
Liquid ammonia density	$\rho_l = 1002.7 - 1.3346 \cdot T$
Thermal conductivity	$k_g = 6.892 \cdot 10^{-7} \cdot T^2 - 2.317 \cdot 10^{-4} \cdot T + 3.578 \cdot 10^{-2}$
	$k_l = 4.697 \cdot 10^{-8} \cdot T^3 + - 4.533 \cdot 10^{-5} \cdot T^2 + 1.229 \cdot 10^{-2} \cdot T - 0.4092$
Specific heat at constant pressure	$C_{p_g} = 9.608 \cdot 10^{-2} \cdot T^2 - 37.19 \cdot T + 5686$
	$C_{p_l} = 3.683 \cdot 10^{-2} \cdot T^2 - 16.63 \cdot T + 5858$
Viscosity	$\mu_g = 1.985 \cdot 10^{-11} \cdot T^2 + 1.992 \cdot 10^{-8} \cdot T + 2.147 \cdot 10^{-6}$
	$\mu_l = 2.076 \cdot 10^{-8} \cdot T^2 - 1.322 \cdot 10^{-5} \cdot T + 2.226 \cdot 10^{-3}$

multiplier r_f=1000 in the pipe flow compared to almost quiescent liquid conditions in the tank for the simulations focused on achieving grid independence.

The average CV size in the storage tank and piping system was halved during each grid refinement. Table 3 gives the number of CVs and simulation time for each of the three grids. Simulations were performed using 128-core Dell PowerEdge R6525 workstations with AMD EPYC 7702 dual 64-core processors.

Fig. 7 demonstrates the results of grid sensitivity analysis by comparing the simulation of pressure dynamics in the storage tank and the connected piping system monitored using the experimental pressure transducers P1, P2 and P3. The simulated pressure dynamics with the coarse mesh (Mesh#1) exhibits >7.7 % deviation from the experimental data and simulations on two other grids. The simulated pressure dynamics for the intermediate (Mesh#2) and fine (Mesh#3) grids are practically identical and closely match the experiment, indicating that grid independence has already been achieved for Mesh#2 with 317,260 CVs. Therefore, considering the computational resources and time required to simulate the full duration of the 560 s experiment, the intermediate Mesh#2 was used further in this study for the model calibration and sensitivity analysis.

4.2. Time step sensitivity analysis

Fig. 8 presents the time step sensitivity analysis using the results of pressure dynamics monitored by sensor P2 before manual valve MV2 during the first 100 s. The simulations were performed with the intermediate mesh (Mesh#2) of 317,260 CVs and time steps ranging from 1 to 100 ms. To assess the influence of time step sensitivity, the additional mass transfer multiplier 'r_f' was again set to 1000.

Large pressure fluctuations are observed with a time step of 100 ms. Minimal variation of simulated pressure dynamics is observed when the time step was reduced from 10 ms to 1 ms, and the simulations closely match the experimental data, having larger oscillations of pressure than in simulations. Simulations with time steps in the range of 1–10 ms are close to each other and experimental pressure dynamics, while the large time step of 100 ms results in higher average pressures and large pressure oscillation amplitudes. Thus, time step 10 ms was chosen as the time step in follow-up simulations. The ammonia mass imbalance was monitored from the simulation every time step, and the imbalance was within acceptable 0.13 %.

The accuracy of simulations to reproduce experimental data is assessed using two indicators: mean relative bias (MRB) and mean relative square error (MRSE) [40,41]. The MRB indicates the CFD model's tendency to overestimate or underestimate, with a value of zero representing a perfect prediction [45]. The MRB quantifies the average deviation between experimental, C_{exp}, and simulated, C_{sim}, values of pressure normalised by their mean:

$$MRB = \left\{ 2 \cdot \frac{C_{exp} - C_{sim}}{C_{exp} + C_{sim}} \right\}. \quad (18)$$

In contrast, the MRSE measures the scattering of squared discrepancies between the experiment and CFD simulations normalised by the square of their mean [44]. Unlike MRB, the MRSE does not cancel out overestimation or underestimation, providing a more comprehensive error assessment for the model prediction [45]:

Table 3
Number of CVs in a grid and corresponding CPU time.

Numerical grid	Total number of CVs in the computational domain	CPU time (560 s)
Coarse (Mesh#1)	151,110	5.8 days
Intermediate (Mesh#2)	317,260	7.3 days
Fine (Mesh#3)	522,230	16 days

$$MRSE = \left\{ 4 \cdot \frac{(C_{exp} - C_{sim})^2}{(C_{exp} + C_{sim})^2} \right\}. \quad (19)$$

Fig. 9 presents log-log plots comparing the effect of time step on the accuracy of simulations to reproduce experimental data using MRB and MRSE. These error metrics were calculated for each simulation over a 100 s flow period.

The simulated accuracy trend follows a similar pattern for both MRB and MRSE, indicating improved accuracy with the time step below 10 ms. However, this comes at the cost of increased computational expense. Thus, there is a trade-off between accuracy and the total time required for simulating the full release period, as smaller time steps demand higher computational resources and time. There is little to no change in MRB and MRSE with a reduction in time step below 10 ms. Thus, 10 ms is chosen as the time step in the follow-up simulations.

4.3. CFD model calibration by time relaxation parameter and modified mass source term

The mass source term in the phase change rate equation in this study is modified from the original time relaxation parameter "r" to the parameter to include the additional multiplier r_f as per Eq. (16a) and Eq. (16b). The multiplier varies gradually the mass transfer rate between phases depending on the volume fraction of liquid and gaseous ammonia. This modification to the mass source term is applied to the pipe and atmospheric regions. The purpose of this modification, as detailed in the section "*Phase change mechanism*", is to account for the unresolved simulation complexities related to intensified boiling and the dynamics of bubbles/droplets associated with changing interfacial area density between the phases.

This work studied three different multiplier profiles for modifying the mass source term in the pipe and atmosphere to demonstrate the variation of the developed methodology in incorporating the modification to the existing time relaxation parameter.

Fig. 10 (top) shows three different profiles for the multiplier r_f as a function of vapour ammonia volumetric fraction and the corresponding pressure dynamics in sensors P2 and P3 in the connected piping system. For demonstrating the effect of three different multiplier r_f profiles, the authors fixed the maximum achieved value of multiplier r_f equal to 1000 to demonstrate the sensitivity of numerical solution to each of multiplier profiles.

The simulated pressure dynamics demonstrated in Fig. 10 (middle) and Fig. 10 (bottom) with the multiplier r_f profiles reaching a limiting value of 1000 at a higher vapour volume fraction in the two-phase mixture flow (profiles 1 and 3) reproduce closely the experimental pressure transients. Yet, profile 1 is better at reproducing pressure dynamics at the beginning of the process. In profile 1, the multiplier "r_f" is set to 1 in the release system and atmospheric region when the vapour fraction is 0.0, i.e., $\alpha_g = 0$ and $\alpha_l = 1$, then it reaches 1000 when the vapour fraction becomes equal to 0.01, then this maximum value is conserved until the vapour fraction increases to 0.99, and afterwards it reduces to r_f=1 when the vapour volume fraction tends to 1, i.e. when liquid ammonia in the flow is fully evaporated.

In contrast, the higher fractions of liquid corresponding to reaching the limiting value of the multiplier, i.e. lower vapour volume fraction of two-phase mixture, in the modified mass source term, i.e. r_f profile 2, results in the damping of the flash boiling in the pipe and thus in unacceptable overprediction of the pressure drop. These findings support the explanation that an increase in the volume fraction of vapour, α_g, within the two-phase mixture leads to an increase in interfacial area density and, consequently, a higher mass transfer rate between the phases. The observations described above imply that maximum mass transfer rates are observed at higher limiting volume fractions of the vapour phase, i.e., when there is a higher vapour volume fraction in the two-phase mixture. This results in a greater interfacial density, which

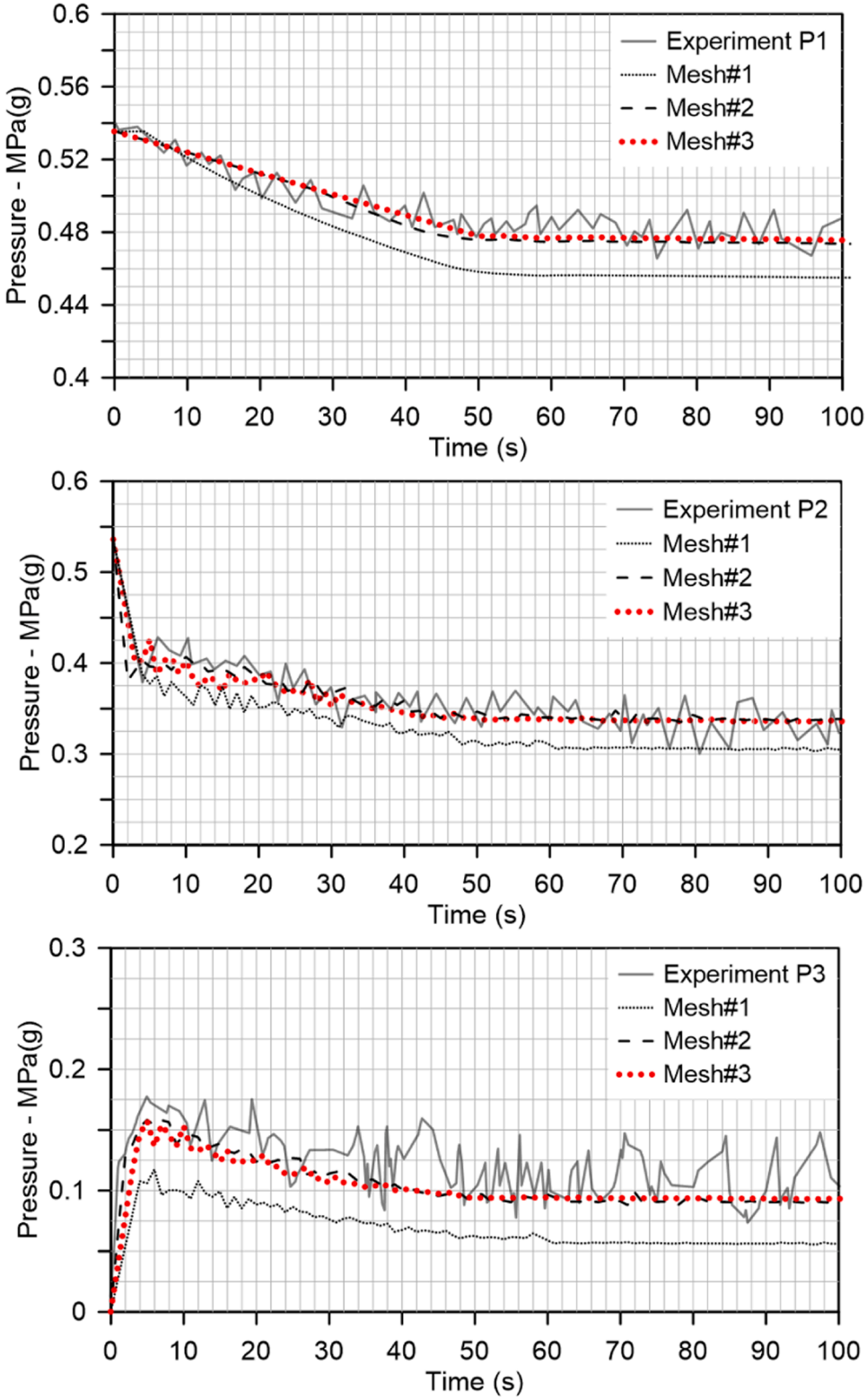

Fig. 7. Effect of grid resolution on the pressure dynamics at sensors P1 (top), P2 (middle) and P3 (bottom). *Note: simulations are performed for the maximum value of the multiplier r_f=1000 (profile 1, see below) and a time step of 10* ms.

enhances mass transfer between the liquid and vapour phases as the flow transitions to a mist or dispersed flow regime at a higher vapour volume fraction.

Using the inverse problem method, the authors examined the sensitivity of the original time relaxation parameter "*r*" and the maximum value for the additional multiplier "r_f" to accurately reproduce the experimentally observed pressure and temperature dynamics in the tank-piping-atmosphere system. This method ensures that the CFD model reliably captures the heat and mass transfer processes during the liquid ammonia release through piping to the atmosphere.

Fig. 11 illustrates the pressure dynamics at sensors P1, P2, and P3, guiding the determination of optimal values for both the time relaxation

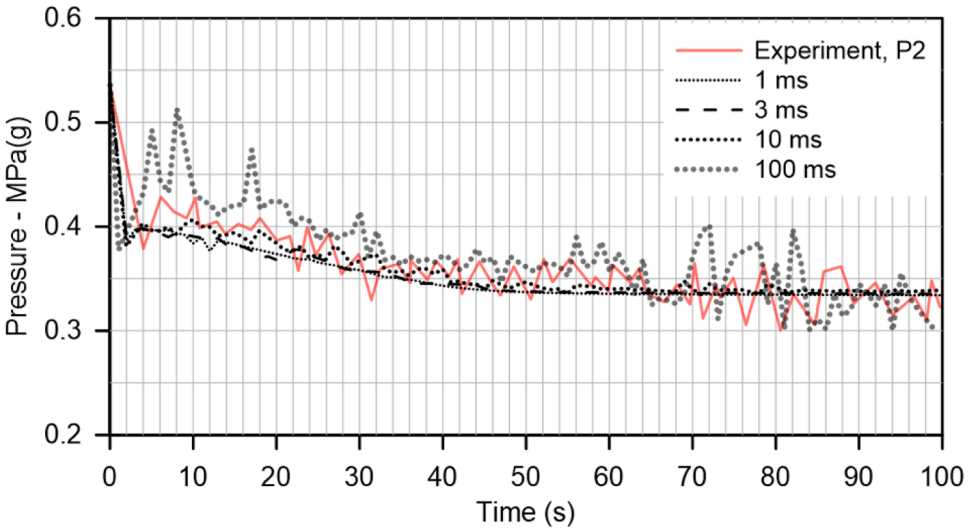

Fig. 8. Time step sensitivity analysis: pressure dynamics at the location of sensor P2 for Mesh#2.

parameter in the tank "r" and the multiplier to it "r_f" in the piping system and the atmosphere by comparing simulations against the experimental data. The piping system multiplier "r_f" was initially set to 1 in the connected hose and pipe system, then increased to its maximum value as the vapour fraction reached in simulations 0.01 (at a distance equal to 0.5 m, equivalent to ten times the pipe diameter from the tank entrance to the piping). Then, "r_f" was held constant until the increasing in time vapour fraction reached 0.99, and afterwards linearly reduced back to 1 as the liquid is fully evaporated. The best reproduction of experimental pressure transients in the tank (P1), the piping system (P2), and the nozzle (P3) is achieved for the time relaxation parameter in the tank of $r = 0.015$ and the multiplier to the time relaxation parameter in the pipe $r_f = (1–300–1)$, i.e. the maximum value of the time relaxation parameter in the pipe of $r_f \cdot r = 0.015 \times 300 = 4.5$.

The sensitivity analysis, conducted by the inverse problem method, has demonstrated that the optimal parameters for simulations of the multiphase flow during the release of liquid ammonia from the storage tank to the atmosphere via the piping system in the considered test are as follows. The optimum time relaxation parameter in the tank is $r = 0.015$ s^{-1} (twice higher than the value 0.007 in our previous study with ammonia vapour, not bulk liquid release from a similar tank ullage space). The optimum multiplier "r_f" varied from 1 at the pipe entrance to its maximum of 300 before returning to 1 as the vapour phase volume fraction dynamically evolved during flash boiling in the piping system as described above. This configuration provided the most accurate validation of the simulated pressure dynamics against experimental data, with an overall deviation of only −1.26 % at P1, +0.6 % at P2, and −1.15 % at P3. Simulations with $r = 0.100$ s^{-1} and $r_f = (1–200–1)$, i.e. with the maximum value of time relaxation parameter in the pipe of $r_f \cdot r = 20$, expectedly overpredict pressure in all three locations. Contrary, simulations with smallest $r = 0.007$ s^{-1} in the pipe and largest $r_f = (1–700–1)$ in the pipe, i.e. with the maximum value of time relaxation parameter in the pipe of $r_f \cdot r = 4.9$, underpredict pressure dynamics for all three pressure transducers. It must be underlined that defining the proper values for the tank and the piping is important. Indeed, the last simulations with a higher total value of $r_f \cdot r = 4.9$ give lower pressure compared to an optimised selection of $r_f \cdot r = 4.5$.

Employing the optimal parameters identified above also resulted in a total released mass of 2405 kg over 560 s, which only slightly deviates from the experimentally measured total mass by +2.22 %. This is well within the acceptable level of accuracy for numerical simulation of multiphase problems of such a level of complexity.

Fig. 12 shows the comparison between the simulated temperature transients for all seven thermocouples T1–T7 against the experimental data, using the optimal parameters identified earlier, i.e. $r = 0.015$ s^{-1} in the tank and the multiplier "r_f" varying from 1 to a maximum of 300, before returning to 1 as the vapour phase volume fraction dynamically evolved with time, $r_f = (1–300–1)$. The simulations correctly reproduce the experimental temperature dynamics for all the thermocouples T1-T7 with a maximum deviation of only +0.11 % (*T1*), +0.45 % (*T2*), −0.02 % (*T3*), −0.043 % (*T4*), +0.0053 % (*T5*), +0.75 % (T6) and +0.52 % (T7).

By adopting the optimal parameters identified above, the model successfully captured the heat and mass transfer processes in the multiphase flow during the release of liquid ammonia into the atmosphere. This includes accurately representing the cooling effect of evaporation at the release nozzle location driven by the endothermic boiling process enhanced by flow expansion after MV2, which is evident by T6 and T7 thermocouples readings.

In the experiment [23], the physical thermocouples T6 and T7 are inserted into the centre of the release pipe. The model exhibited minimal deviation from the experimental data, with T6 showing a deviation of only +0.75 % and T7 demonstrating a deviation of +0.52 %. This effectively replicates the cooling effect associated with evaporation, including the subsequent temperature drop and recovery.

During the numerical experiments, it was observed that using a higher value of $r_f \cdot r$ in the piping system led to excessive evaporation upstream of the nozzle. This reduced the amount of liquid ammonia reaching the nozzle to a negligible value, thus "eliminating" the experimentally observed cooling effect of evaporation (resulting in higher simulated temperatures at the T7 location, as there was insufficient amount of liquid to vaporise and decrease the flow temperature). Fig. 13 demonstrates the reproduction of the cooling effect in the release nozzle by comparing two different total values of the modified time relaxation parameter.

The insights from this validation study underline the importance of proper calibration of the time relaxation parameter "r" in the tank and the multiplier "r_f" in the pipe. Through the inverse problem method employed, the parameters identified can be deemed optimal for simulating heat and mass transfer in the tank-piping-atmosphere system. These parameters effectively capture the complex multiphase system pressure (3 sensors) and temperature (7 sensors) dynamics observed during liquid ammonia depressurisation scenarios. This approach ensures accurate predictions of flashing behaviour during multiphase flow during incidental leakages of liquid ammonia to the atmosphere and is planned to be used for simulations of bunkering as the experimental data are made available.

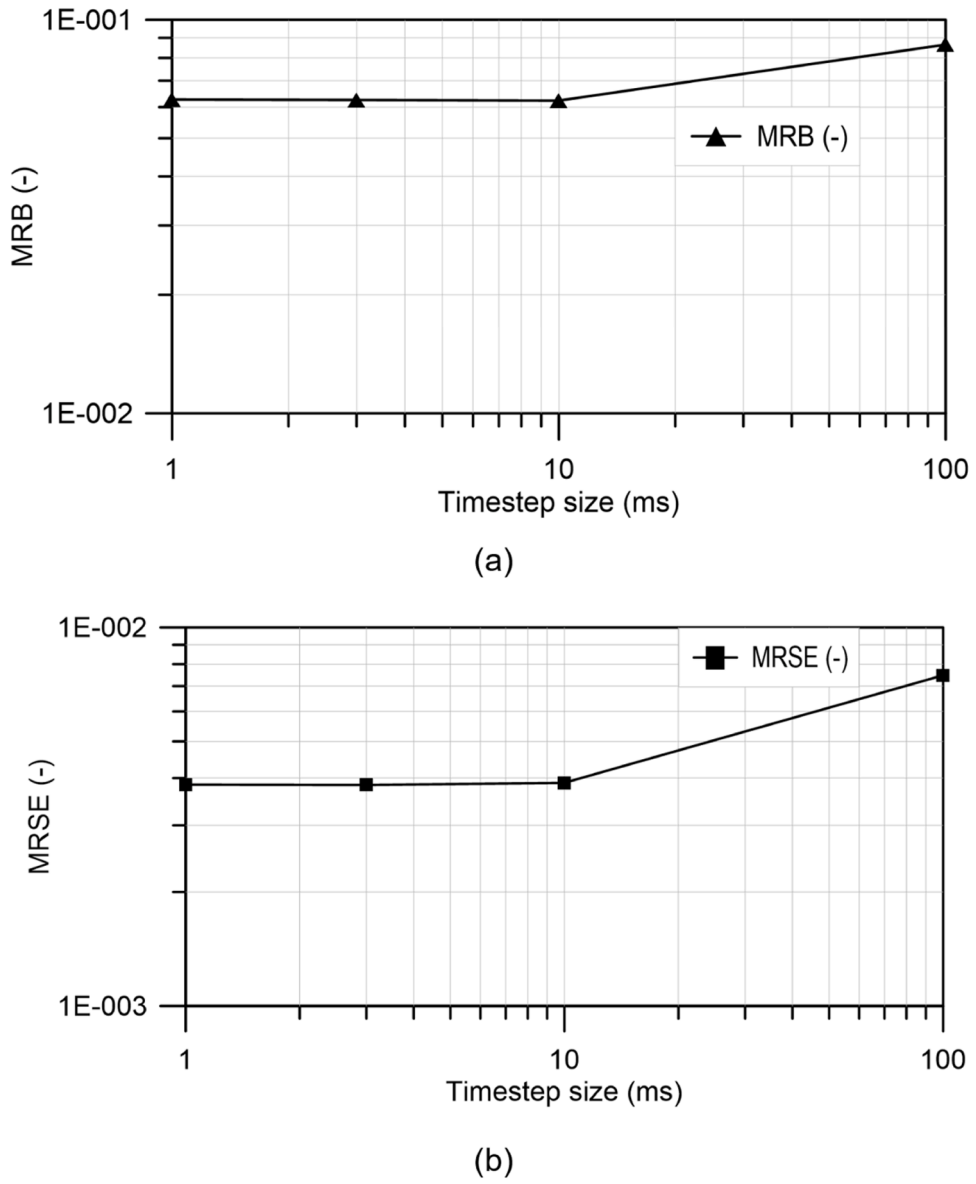

Fig. 9. Time step sensitivity analysis: (a) - mean relative bias, (b) - mean relative square error.

Fig. 14a illustrates the liquid phase volume fraction in a cross-sectional view of the ammonia tank, highlighting the liquid boiling mechanisms at four time instances as liquid ammonia is released through the connected piping system to the atmosphere. While the vapour volume fraction at the pipe entrance from the tank is 0.0 at time 0 s, it increases at the same location to 0.55 at 560 s (see Fig. 14b). Fig. 14b depicts the distribution of liquid ammonia fraction in a central sectional cut along the diameter of the connected piping system at different locations.

As observed from the cross-sectional view of the ammonia tank (see Fig. 14a), the volume fraction of vapour ammonia increases, indicating liquid ammonia boiling in the tank volume due to pressure reduction. The gradual rise in vapour fraction within the liquid bulk signifies the ongoing generation and formation of vapour inside the liquid phase due to boiling as the depressurisation continues. Consequently, the variation in vapour fraction across the tank reflects the dynamic interplay of bubble generation, rise, growth, and coalescence during the depressurisation process.

The uniform distribution of the liquid phase in the central sectional cut across the diameter (see Fig. 14b) is representative of the highly turbulent flash boiling flow within the piping system. In such flow, the existing, in reality, a velocity shift between phases and turbulence overcomes the cohesive forces at the liquid-vapour interface, leading to the fragmentation of the liquid into fine droplets. This fragmentation enhances the dispersion of the liquid phase uniformly throughout the gas phase as bubbles or droplets, thus promoting effective mixing. The resulting interaction between the gas and liquid phases significantly influences and enhances the heat and mass transfer processes between the phases.

Fig. 15 illustrates the mass transfer rate and the static pressure along the pipe's centreline at four different flow times, demonstrating consistency along the pipe length after some initial fluctuations. The appropriateness of centreline values is supported by the uniform phase distribution demonstrated in Fig. 14. This stabilisation reflects quasi-steady flow conditions, where the pipe's turbulence and phase interactions sustain flash boiling, leading to increased mass transfer (evaporation) in elements of piping systems of reduced internal diameter where the increase of flow velocity results in the local decrease of

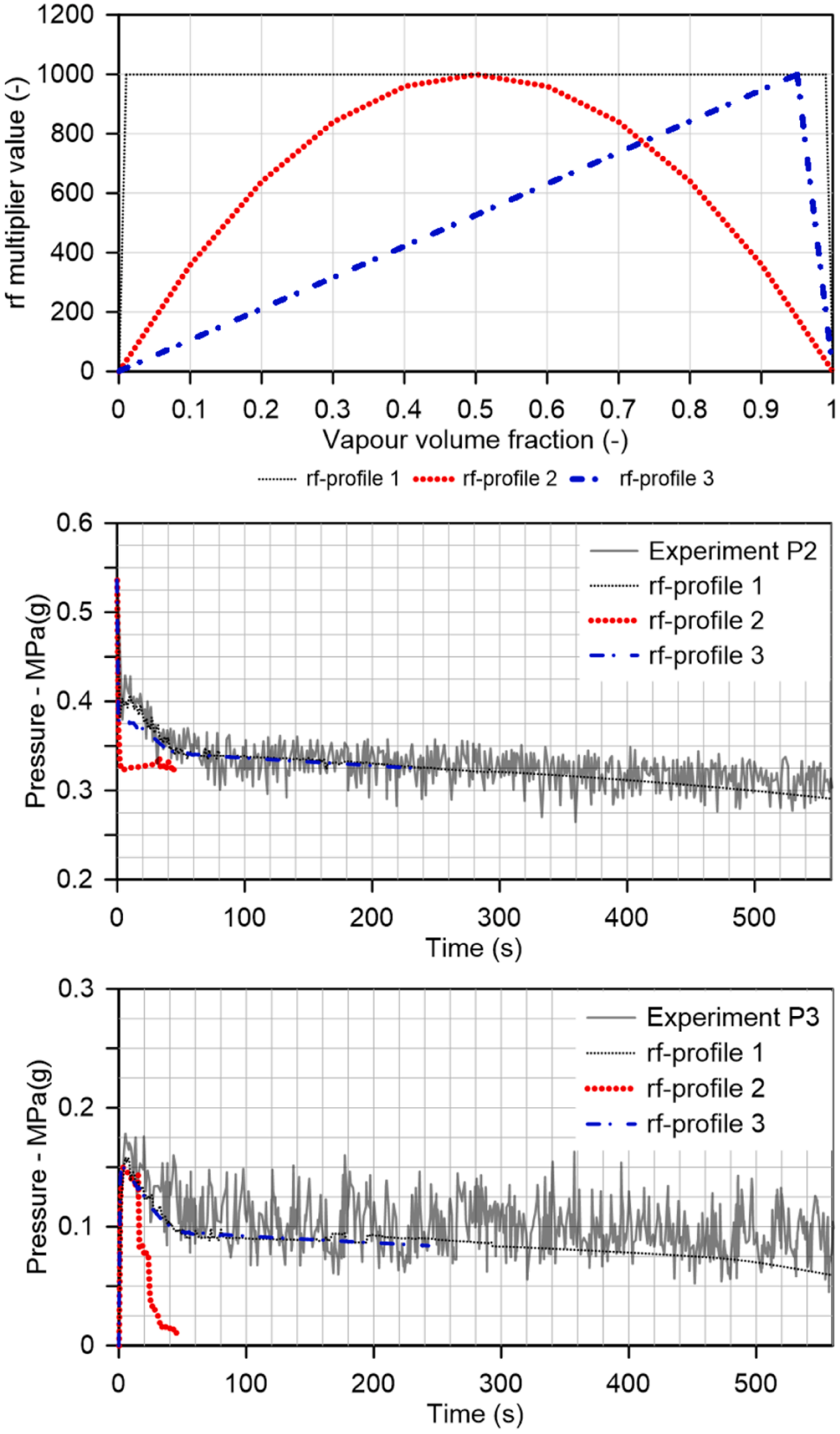

Fig. 10. Sensitivity analysis of simulations results to different profiles of multiplier r_f with the same maximum value of 1000. Top - three multiplier profiles r_f at different limiting liquid ammonia volume fractions. Middle: pressure dynamics at the location of sensor P2. Bottom: pressure dynamics at sensor P3.

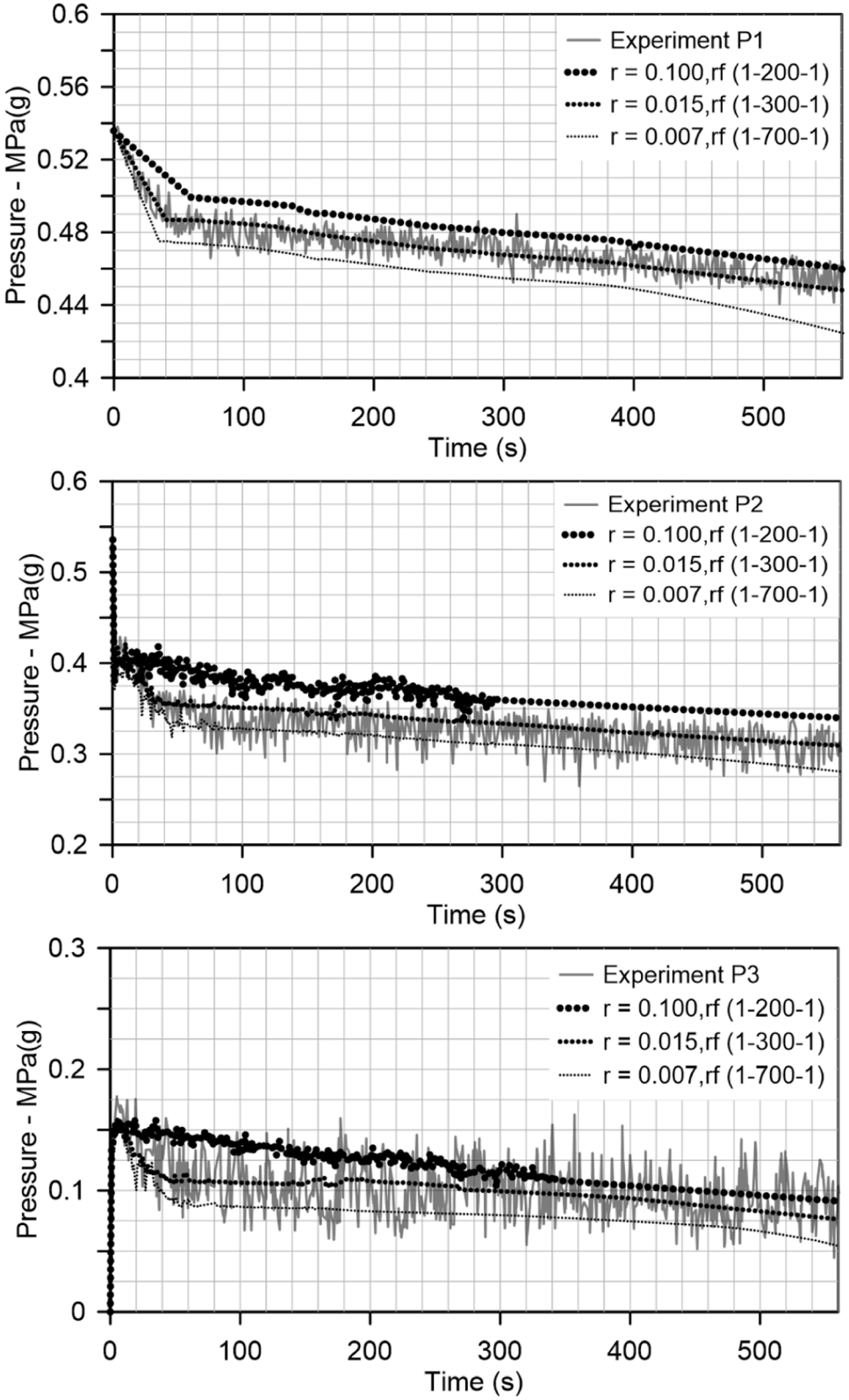

Fig. 11. Effect of the time relaxation parameter "r" and the multiplier "r_f" on the pressure dynamics at sensors P1 in the tank (top), P2 in the piping (middle), and P3 in the nozzle (bottom). *Note: simulations are performed for the multiplier r_f profile 1.*

pressure due to the continuity equation. The positive net mass transfer rate confirms that evaporation is the dominant phase change, aligning with the principles of flash boiling.

4.4. Multiphase flow characteristics in the release nozzle and nearby area in the atmosphere

While this study does not examine the dispersion of flashing liquid ammonia released into the atmosphere, it remains crucial to understand

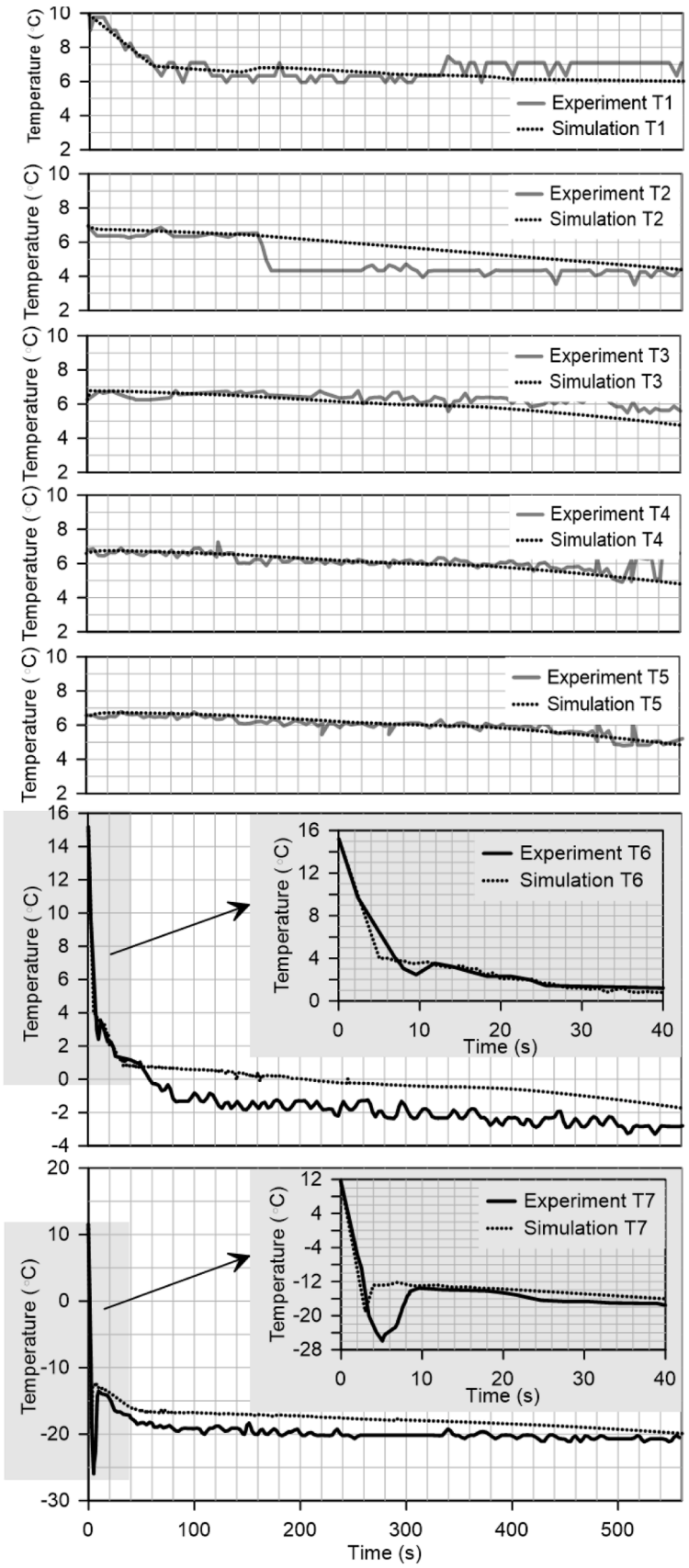

Fig. 12. Comparison of experimental and simulated temperature transients in thermocouples T1–T7. *Note: simulations are performed for the multiplier r_f profile 1, using $r = 0.015$ and $r_f = (1–300–1)$.*

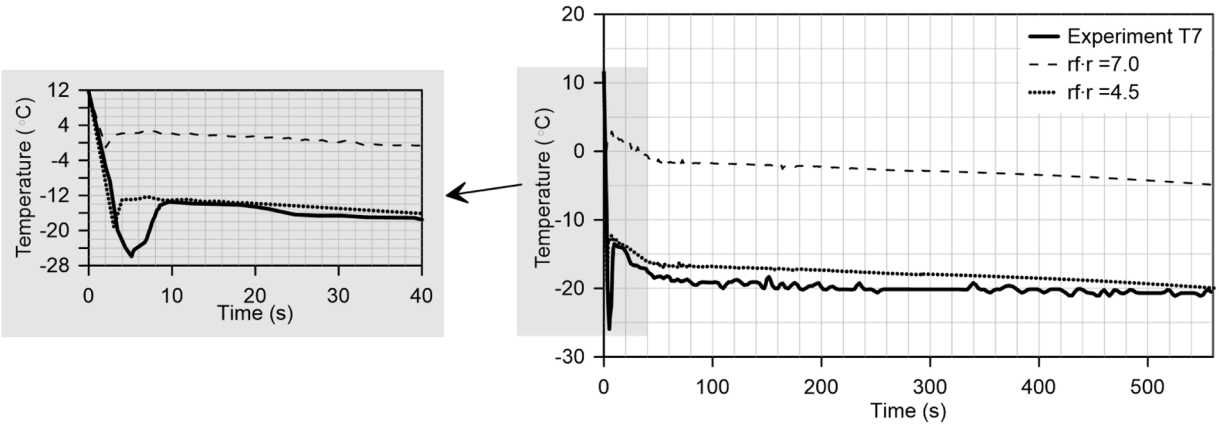

Fig. 13. Comparative analysis of the cooling effect within the release nozzle under two different maximum values of the time relaxation parameter $r_f \cdot r$ in the piping system.

the key characteristics of the two-phase flow at the nozzle exit. This knowledge is important for future safety engineering research requiring release source term modelling.

In the context of two-phase flow, one of the critical parameters is the sound velocity. The complex interactions between the phases influence the speed of sound and the dynamics of flow. In two-phase flow, the speed of sound is significantly lower than in a single-phase vapour due to the presence of the liquid phase, which contributes to higher density and altered compressibility [46,47]. This phenomenon is particularly relevant in scenarios of choked flow, where the flow reaches a maximum velocity, limited by the speed of sound in the medium. The two-phase flow velocity is also influenced by the vapour quality, which represents the ratio of the mass of the gas phase to the total mass of the mixture. As the flow exits to the atmosphere, this void fraction varies dynamically depending on the phase change characteristics, affecting the overall flow behaviour and sound speed propagation. The interactions between the liquid droplets and the gas phase are vital, as they can influence energy and momentum transfer, potentially due to evaporation or condensation of droplets.

Fig. 16 illustrates a view of the release nozzle and nearby areas in the atmosphere. The nozzle is positioned 1.015 m above the ground level. This figure presents the contour plots of the mole fraction of gaseous ammonia, the mole fraction of air, the liquid ammonia volume fraction of the releasing mixture, and the velocity field near the nozzle.

As seen from Fig. 16 (top-left), the two-phase mixture is primarily composed of vapour, aligning with previous observations in Fig. 14, where the maximum liquid phase volume fraction at the nozzle exit remained below 7 %. At the nozzle exit, the flow was observed to be predominantly vapour, with a maximum vapour phase volume fraction of 0.923 (refer to Fig. 16). Upon release to the atmosphere, the ammonia jet is diluted by the air entrainment, causing a reduction in ammonia vapour fraction downstream of the nozzle as shown in Fig. 16 (top-right).

The maximum liquid fraction of 7 % in the jet was observed close to the nozzle exit surface, at less than one nozzle diameter. This fraction decreased rapidly due to evaporation as the jet was released into the atmosphere, with all liquid ammonia in the mixture (see Fig. 16, bottom-left) completely evaporating at about 13.91 m downwind from the release source. The liquid phase introduces substantial changes to the flow dynamics through added mass and momentum transfer between the phases. Fig. 17 demonstrates the centreline velocity distribution and the liquid fraction as a function of distance just 0.5 m before and after the exit nozzle surface at one flow time instance ($t = 50$ s).

Fig. 17 demonstrates the increase in flow velocity within the nozzle accompanied by the evaporation of liquid ammonia, evidenced by the reduction in liquid phase volume fraction. The continuous evaporation of the liquid phase enables the flow to accelerate under mass and momentum conservation principles. At the nozzle exit, depressurisation into the open atmosphere amplifies this effect, as the vapour phase experiences further acceleration for a short distance, after which the velocity starts to decrease due to air entrainment.

In a two-phase mixture, the speed of sound could be significantly lower compared to that in a pure gas. This is due to the increased density and the liquid phase's effect on compressibility. The liquid droplets generate drag and inertia, altering the overall velocity distribution. These droplets resist acceleration more than the vapour, resulting in a velocity differential between the phases. This interaction ultimately results in the velocity of the two-phase flow being less compared to the pure gaseous flow of the same substance.

This was observed in the simulations (Fig. 16, bottom-right) that despite the presence of only a little liquid fraction (below 7 % at the nozzle exit), its presence significantly reduces the speed of sound to below 100 m/s. Indeed, the speed of sound in pure gaseous ammonia can be calculated for the same conditions at the nozzle exit:

$$C = \sqrt{\frac{\gamma \cdot P}{\rho}} = \sqrt{\frac{1.31 \cdot (213625\ Pa)}{1.81\ kg/m^3}} = 393.21\ m \Big/ s, \tag{20}$$

where γ is the ratio of specific heat ($\gamma = c_p/c_v = 1.31$ for ammonia); here, the pressure was taken from the numerical solution at the nozzle exit, and the density was taken for the pure gaseous ammonia (gNH_3) at the temperature at the nozzle exit, i.e. 256.5 K. The speed of sound in pure gaseous ammonia is 393.21 m/s, almost four times higher than in two-phase flow (Fig. 16, bottom-right).

Additionally, the droplets may induce flow instabilities, potentially leading to turbulence and velocity fluctuations. These complexities highlight the intricate nature of two-phase flow dynamics, where even a minor liquid fraction can have substantial effects on velocity and other flow properties. Accurately understanding these dynamics is critical for predicting two-phase release behaviour, particularly in safety-critical scenarios like ammonia releases during containment failures.

The obtained in CFD simulations of two-phase mixture velocity in the nozzle was compared against the theoretical speed of sound, C, available in the literature for two-phase mixtures, as detailed in Table 4.

In Eq. (21) in Table 4, $V = x \cdot V_g + (1 - x) \cdot V_l$ is the specific volume of the mixture and $V_{fg} = V_g - V_l$; x is the vapour quality, which is the ratio of the mass of the gas phase to the total mass of the mixture, V_g and V_l are the specific volumes of gas and liquid phases, respectively. Using Eq. (21), which utilises the mixture properties at different time instances, the derivatives were calculated to determine the two-phase mixture velocity at the nozzle exit. In Eq. (22), $C_g = 394$ m/s and $C_l = 1630$ m/s indicate the speed of sound for pure gaseous and liquid ammonia, respectively, obtained from the NIST database [30] for

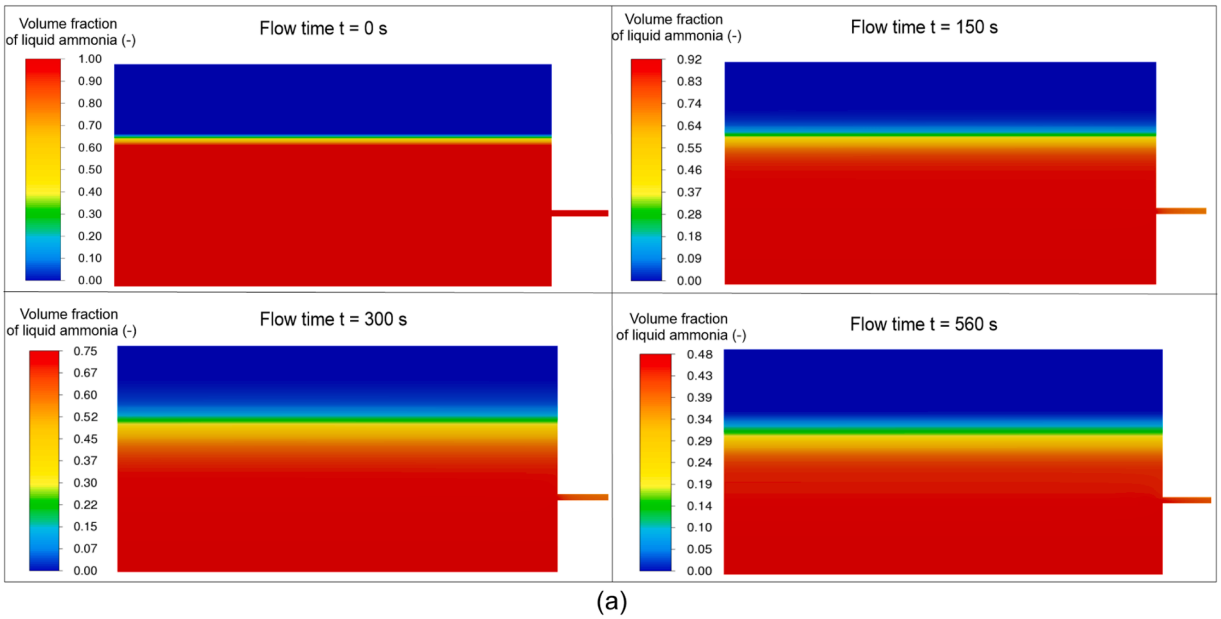

(a)

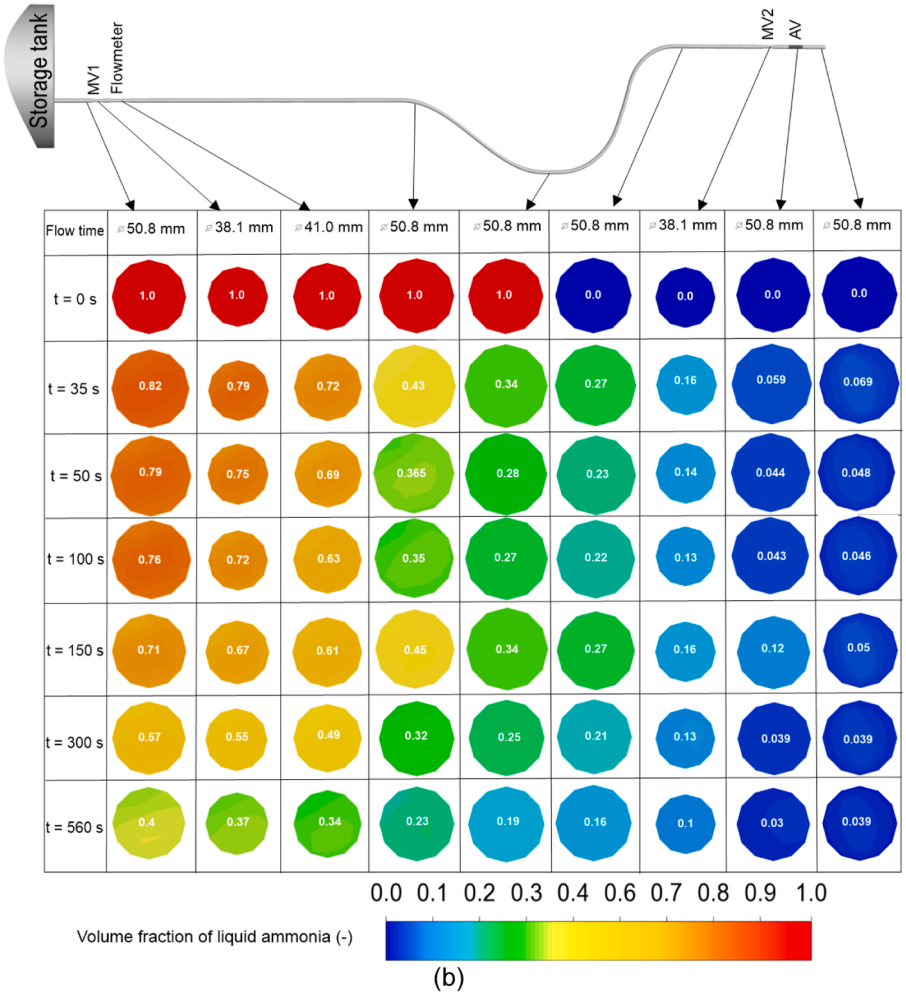

(b)

Fig. 14. Time history of multiphase flow in liquid ammonia release: (a) - cross-sectional view of liquid fraction in ammonia tank during depressurisation (note: the upper limit of liquid ammonia fraction, i.e. its maximum value, is decreasing with time); (b) - central section showing uniform liquid fraction distribution across various points in the piping system. *Note: The contour plots in Fig. 14b illustrate the maximum liquid volume fraction at each respective point.*

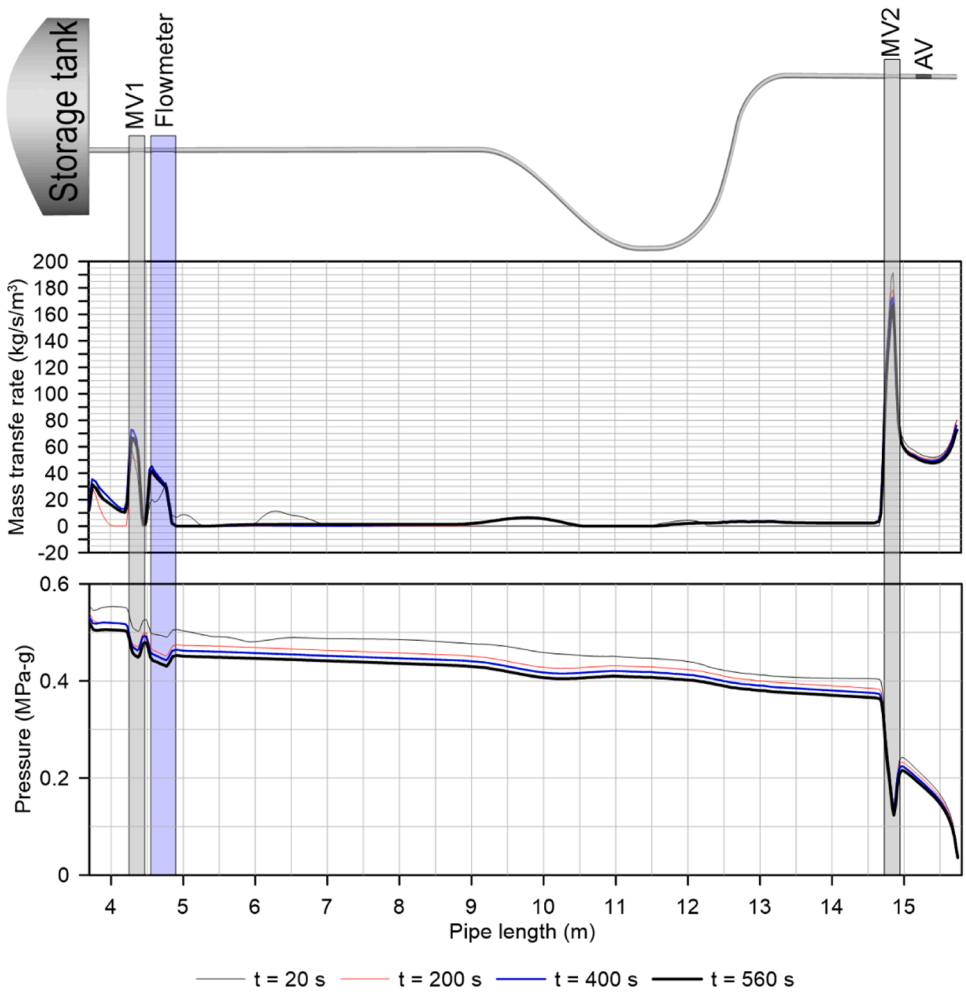

Fig. 15. Simulated values of mass transfer rate between phases (top) and static pressure (bottom) along the centreline of piping system.

corresponding pressure and temperature conditions. The two-phase mixture velocity of the choked flow at the nozzle exit, predicted by CFD simulations as 90.2 m/s (see Fig. 16, bottom-right) aligns closely with the theoretical speed of sound calculated using both literature expressions shown in Table 4. This agreement demonstrates the robustness of the developed CFD model in capturing the flashing behaviour across the entire system, ensuring its reliability for simulating incidental leakage and dispersion scenarios.

5. Conclusions

This study conducted a numerical investigation of heat and mass transfer during the dynamic flash boiling in the system of the ammonia storage tank and piping systems during release to the atmosphere. The *originality* of this paper lies in multiphase modelling for the first time of internal and external flash boiling of liquid ammonia in the tank-piping-atmosphere system. The VOF method, integrated with a modified evaporation/condensation model, is applied to simulate heat and mass transfer phenomena during release from liquid ammonia storage. The proposed phase change mechanism varies the mass transfer rate based on the volume fractions of liquid and gaseous ammonia in a control volume. This accounts for the unresolved complexities associated with the influence of interfacial area density in two-phase mixtures. The essential increase of the time relaxation parameter is observed in the piping compared to the storage tank. This is due to the increase of liquid-vapour interface in high-velocity piping flow compared to almost quiescent conditions of flow in the storage tank.

This study's *significance* lies in developing a multiphase CFD model that includes a UDF for a modified phase change mechanism and can accurately reproduce experimentally measured pressures (3 locations) and temperatures (7 locations) transients. This model accurately and efficiently simulates heat and mass transfer and system dynamics throughout the release period of 560 s. The analysis highlights the importance of flash boiling being the primary driver of the cooling effect within the release system and nozzle. Insights from this research can contribute to the design of inherently safer ammonia storage tank management while supporting future studies in the sense of the source term modelling for safety engineering applications. The model can be applied to the development of ammonia bunkering protocols. It will be done after the model validation as soon as experimental data on ammonia bunkering are made available.

The *rigour* of this study is evident from the comprehensive validation campaign undertaken. The developed model was validated against experimental data from INERIS, accurately reproducing pressure and temperature dynamics in the storage tank, release piping and nozzle. The model successfully captures the heat and mass transfer phenomena, including the cooling effect of evaporation in the nozzle that is found to be sensitive to the value of the time relaxation parameter. The extensive numerical experiments of model calibration were performed to investigate the influence of the time relaxation parameter in the tank r and the multiplier r_f in the piping for the modification of mass source term in the evaporation/condensation model. The numerically obtained in CFD simulations speed of sound in a two-phase mixture of gaseous and liquid ammonia was in close agreement with available theoretical values.

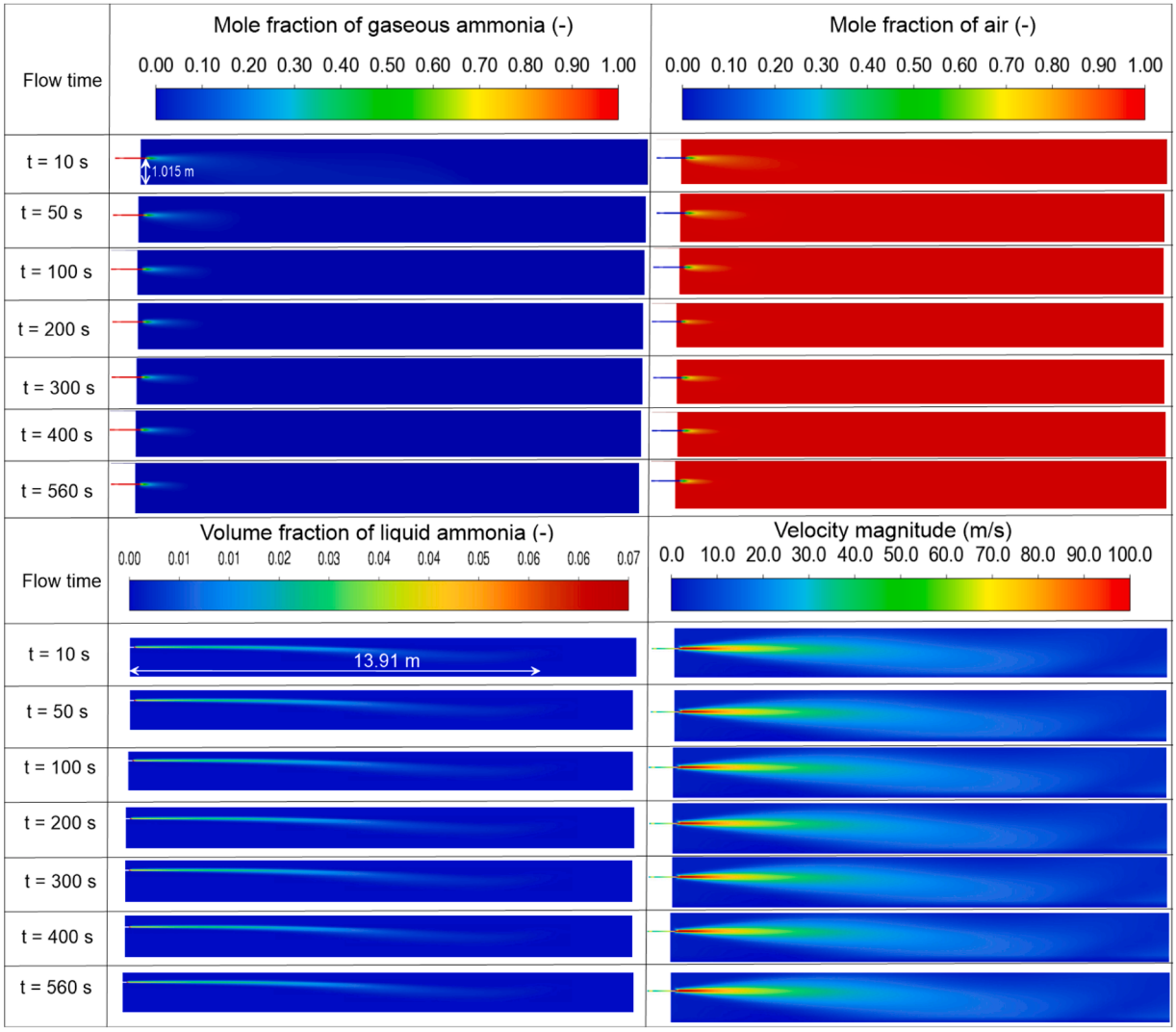

Fig. 16. Cross-section view around the release nozzle: mole fraction of gaseous ammonia (top-left), mole fraction of air (top-right), liquid ammonia volume fraction (bottom-left), and two-phase flow velocity (bottom-right).

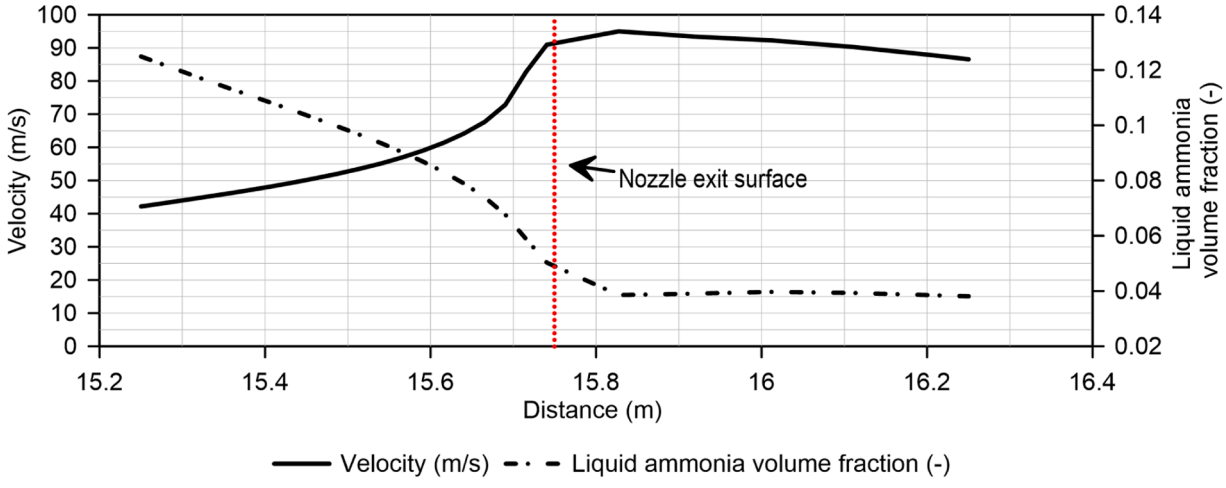

Fig. 17. Demonstration of centreline velocity profile and liquid ammonia volume fraction close to exit nozzle surface at $t = 50$ s.

The findings demonstrate that precise heat and mass transfer representation is critical for understanding the multiphase flow dynamics in flash boiling scenarios. This is essential for future modelling of ammonia release and dispersion in the atmosphere to define hazard distances in arbitrary loss-of-containment incidents and the development of ammonia bunkering protocols. This underpins the practical importance

Table 4
The theoretical speed of sound expressions available in the literature for two-phase mixtures.

Theoretical speed of sound	Calculated value (m/s)	Reference
$C^2 = \frac{\frac{V^2}{T^2}\cdot\left(\frac{L_H}{V_{fg}}\right)^2}{\frac{cp_l}{T} + x\cdot(V_{fg})\cdot\frac{d}{dT}\left(\frac{L_H}{T\cdot V_{fg}}\right) - \frac{L_H}{T\cdot V_{fg}}\frac{dV_l}{dT}}$ (21)	86.8	[48,49]
$\frac{1}{C^2} = \left(\frac{1}{\frac{x}{\rho_g} + \frac{1-x}{\rho_l}}\right)^2 \left(\frac{x}{\rho_g^2 c_g^2} + \frac{1-x}{\rho_l^2 c_l^2}\right)$ (22)	93.4	[50]

of the developed and validated model for safety engineering in alternate energy infrastructures such as bunkering ports and networks.

Future studies will focus on extending the CFD model based on current results to predict the flashing release of liquid ammonia into the atmosphere for dispersion studies at large scales of thousands of meters. The aim will be to develop and validate the CFD dispersion model accounting for real wind conditions to accurately predict hazard distances by toxicity and flammability for unscheduled ammonia release scenarios.

CRediT authorship contribution statement

Vladimir Molkov: Writing – review & editing, Writing – original draft, Visualization, Validation, Supervision, Software, Methodology, Investigation, Funding acquisition, Conceptualization. **Srinivas Sivaraman:** Writing – review & editing, Writing – original draft, Visualization, Validation, Software, Methodology, Investigation, Formal analysis, Conceptualization. **Donatella Cirrone:** Writing – review & editing, Writing – original draft, Visualization, Supervision, Software, Methodology, Investigation, Conceptualization. **Benjamin Truchot:** Writing – review & editing, Writing – original draft, Validation, Supervision, Resources, Methodology, Investigation, Conceptualization. **Dmitriy Makarov:** Writing – review & editing, Writing – original draft, Visualization, Validation, Supervision, Software, Methodology, Investigation, Conceptualization.

Declaration of competing interest

The authors declare that they have no known competing financial interests or personal relationships that could have appeared to influence the work reported in this paper.

Acknowledgments

This research has received funding from the Engineering and Physical Sciences Research Council (EPSRC) of the UK through the Centre for Doctoral Training in Sustainable Hydrogen (SusHy, Grant EP/S023909/1); Tier 2 Northern Ireland High-Performance Computing facility (NI-HPC Kelvin-2, Grant EP/T022175/1). The study is supported by the UK Department for Transport, as part of the UK Shipping Office for Reducing Emissions (UK SHORE) Programme, and the EPSRC (UK National Clean Maritime Research Hub, Grant EP/Y024605/1).

Data availability

Data will be made available on request.

References

[1] D. Miura, T. Tezuka, A comparative study of ammonia energy systems as a future energy carrier, with particular reference to vehicle use in Japan, Energy 68 (2014) 428–436, https://doi.org/10.1016/j.energy.2014.02.108.
[2] Y. Kojima, M. Yamaguchi, Ammonia as a hydrogen energy carrier, Int. J. Hydrog. Energy 47 (2022) 22832–22839, https://doi.org/10.1016/j.ijhydene.2022.05.096.
[3] X. Zhu, X. Pan, J. Ma, Y. Mei, H. Tang, Y. Zhu, L. Liu, J. Jiang, T. Chen, Dynamic behaviors of in-tank subcooled liquid with depressurization-induced phase change and the impact on primary breakup of flashing jet, Int. J. Therm. Sci. 186 (2023) 108118, https://doi.org/10.1016/j.ijthermalsci.2022.108118.
[4] T. Watanabe, Y. Hanaoka, I. Tokura, Flashing phenomena of depressurized liquid nitrogen in a pressure vessel. Part 2: mist formation and behavior of the liquid surface in the early depressurization process, Heat Transf. - Japan. Res. 27 (1998) 327–335, https://doi.org/10.1002/(SICI)1520-6556(1998)27:5<327::AID-HTJ1>3.0.CO;2-X.
[5] M. BENTZ, C. WILKINSON, in: Experimental study of flash boiling in liquid nitrogen, in: 19th Joint Propulsion Conference, American Institute of Aeronautics and Astronautics, Reston, Virigina, 1983, https://doi.org/10.2514/6.1983-1378.
[6] M. Takeda, T. Usui, K. Maekawa, Study on boiling behavior of pressurized liquid nitrogen under rapid depressurization, IOP. Conf. Ser. Mater. Sci. Eng. 502 (2019) 012092, https://doi.org/10.1088/1757-899X/502/1/012092.
[7] D. Saury, S. Harmand, M. Siroux, Flash evaporation from a water pool: influence of the liquid height and of the depressurization rate, Int. J. Therm. Sci. 44 (2005) 953–965, https://doi.org/10.1016/j.ijthermalsci.2005.03.005.
[8] Q. Shang, Z. Tian, S. Wang, M. Hua, X. Pan, S. Shi, J. Jiang, Experimental research on the two-phase explosive boiling mechanism of superheated liquid under different leakage conditions, Appl. Therm. Eng. 216 (2022) 119080, https://doi.org/10.1016/j.applthermaleng.2022.119080.
[9] Z. Tian, Q. Shang, X. Pan, R. Zhang, M. Hua, Y. Zhao, J. Jiang, Experimental study on explosive boiling mechanism of superheated liquid containing ethanol impurities under rapid depressurization, Process Saf. Environ. Protect. 168 (2022) 443–453, https://doi.org/10.1016/j.psep.2022.09.073.
[10] Y. HANAOKA, K. MAENO, L. ZHAO, G. HEYMANN, A study of liquid flashing phenomenon under rapid depressurization, JSME Int. J. Ser. 2, Fluids Eng., Heat Transf., Power, Combust., Thermophys. Properties 33 (1990) 276–282, https://doi.org/10.1299/jsmeb1988.33.2_276.
[11] K. Tani, T. Himeno, Y. Sakuma, T. Watanabe, H. Kobayashi, T. Toge, S. Unno, S. Kamiya, O. Muragishi, K. Kanbe, Pressure recovery during pressure reduction experiment with large-scale liquid hydrogen tank, Int. J. Hydrogen. Energy 46 (2021) 29583–29596, https://doi.org/10.1016/j.ijhydene.2020.12.184.
[12] T. Kangwanpongpan, D. Makarov, D. Cirrone, V. Molkov, LES model of flash-boiling and pressure recovery phenomena during release from large-scale pressurised liquid hydrogen storage tank, Int. J. Hydrog. Energy 50 (2024) 390–405, https://doi.org/10.1016/j.ijhydene.2023.07.126.
[13] S. Sivaraman, D. Makarov, V. Molkov, Flash boiling and pressure recovery phenomenon during venting from liquid ammonia tank ullage, Process Saf. Environ. Protect. 182 (2024) 880–893, https://doi.org/10.1016/j.psep.2023.12.037.
[14] G. Polanco, A.E. Holdø, G. Munday, General review of flashing jet studies, J. Hazard. Mater. 173 (2010) 2–18, https://doi.org/10.1016/j.jhazmat.2009.08.138.
[15] R.D. Oza, J.F. Sinnamon, An experimental and analytical study of flash-boiling fuel injection, SAE Trans. 92 (1983) 948–962.
[16] X. Zhu, X. Pan, H. Tang, X. Wang, Y. Zhu, L.X. Liu, J. Jiang, T. Chen, Breakup regime of flashing jet under thermal nonequilibrium and mechanical forces and its relationship with jet characteristics during depressurized releases of superheated liquid, Process Saf. Environ. Protect. 170 (2023) 757–770, https://doi.org/10.1016/j.psep.2022.12.042.
[17] M. Ahmad, M.B. Osch, L. Buit, O. Florisson, C. Hulsbosch-Dam, M. Spruijt, F. Davolio, Study of the thermohydraulics of CO2 discharge from a high pressure reservoir, Int. J. Greenh. Gas Control 19 (2013) 63–73, https://doi.org/10.1016/j.ijggc.2013.08.004.
[18] X. Zhu, Z. Song, X. Pan, X. Wang, J. Jiang, Pressure-decay and thermodynamic characteristics of subcooled liquid in the tank and their interaction with flashing jets, J. Hazard. Mater. 378 (2019) 120578, https://doi.org/10.1016/j.jhazmat.2019.04.061.
[19] X. Guo, W. Tan, L. Liu, C. Liu, G. Zhu, Experimental study of liquefied gas dynamic leakage behavior from a pressurized vessel, Process Saf. Environ. Protect. 151 (2021) 20–27, https://doi.org/10.1016/j.psep.2021.05.005.
[20] S. Kashkarov, M. Dadashzadeh, S. Sivaraman, V. Molkov, Quantitative risk assessment methodology for hydrogen tank rupture in a tunnel fire, Hydrogen 3 (2022) 512–530, https://doi.org/10.3390/hydrogen3040033.
[21] S. Kashkarov, M. Dadashzadeh, S. Sivaraman, V. Molkov, QRA methodology of hydrogen tank rupture in a fire in a tunnel, in: 10th International Seminar on Fire and Explosion Hazards, 2022.
[22] V. Molkov, S. Kashkarov, S. Sivaraman, D. Makarov, Hazards and associated risks of hydrogen vehicles in underground traffic infrastructure, Chem. Eng. Trans. 105 (2023) 43–48.
[23] Bouet R., Salvi O., Faucher B., AMMONIA large-scale atmospheric dispersion tests, report No. INERIS-DRA-RBo-1999–20410., 2005.
[24] ANSYS, ANSYS Fluent Theory Guide, 2023.
[25] Y. Zhao, Z. Liu, X. Shi, X. Qian, Y. Zhou, D. Zhang, Q. Li, Numerical simulation on BLEVE mechanism of supercritical carbon dioxide, Energy Procedia 75 (2015) 880–885, https://doi.org/10.1016/j.egypro.2015.07.204.
[26] B. He, X.-S. Jiang, G.-R. Yang, J.-N. Xu, A numerical simulation study on the formation and dispersion of flammable vapor cloud in underground confined space, Process Saf. Environ. Protect. 107 (2017) 1–11, https://doi.org/10.1016/j.psep.2016.12.010.

[27] T. Iannaccone, G.E. Scarponi, G. Landucci, V. Cozzani, Numerical simulation of LNG tanks exposed to fire, Process Saf. Environ. Protect. 149 (2021) 735–749, https://doi.org/10.1016/j.psep.2021.03.027.
[28] H.I. Mohammed, P.T. sardari, D. Giddings, Multiphase flow and boiling heat transfer modelling of nanofluids in horizontal tubes embedded in a metal foam, Int. J. Therm. Sci. 146 (2019) 106099, https://doi.org/10.1016/j.ijthermalsci.2019.106099.
[29] Y. Liao, D. Lucas, A review on numerical modelling of flashing flow with application to nuclear safety analysis, Appl. Therm. Eng. 182 (2021) 116002, https://doi.org/10.1016/j.applthermaleng.2020.116002.
[30] NIST, NIST Chemistry Webbook. Thermophysical Properties of Fluid Systems <https://webbook.nist.gov/chemistry/fluid/>, (2024).
[31] W.H. Lee, Pressure iteration scheme for two-phase flow modelling. Multiphase transport: fundamentals, Reactor safety, Applications, 1980.
[32] J. Zhang, W. Li, Numerical study on heat transfer and pressure drop characteristics of R410A condensation in horizontal circular mini/micro-tubes, Can. J. Chem. Eng. 94 (2016) 1809–1819, https://doi.org/10.1002/cjce.22554.
[33] Y. You, G. Wang, C. Guo, H. Jiang, Study on mass transfer time relaxation parameter of indirect evaporative cooler considering primary air condensation, Appl. Therm. Eng. 181 (2020) 115958, https://doi.org/10.1016/j.applthermaleng.2020.115958.
[34] Z. Yang, X.F. Peng, P. Ye, Numerical and experimental investigation of two phase flow during boiling in a coiled tube, Int. J. Heat. Mass Transf. 51 (2008) 1003–1016, https://doi.org/10.1016/j.ijheatmasstransfer.2007.05.025.
[35] L. Teng, X. Liu, J. Bian, Y. Li, C. Lu, A homogeneous relaxation model for multi-phase CO2 jets following the release of supercritical CO2 pipelines, J. Nat. Gas. Sci. Eng. 84 (2020) 103609, https://doi.org/10.1016/j.jngse.2020.103609.
[36] S.C.K. De Schepper, G.J. Heynderickx, G.B. Marin, Modeling the evaporation of a hydrocarbon feedstock in the convection section of a steam cracker, Comput. Chem. Eng. 33 (2009) 122–132, https://doi.org/10.1016/j.compchemeng.2008.07.013.
[37] X. Luan, M. Zhang, S. Zhao, B. Zhang, Numerical study on the effects of bund on liquid pool spreading and vapor dispersion after a catastrophic LNG tank failure, Process Saf. Environ. Protect. 176 (2023) 74–86, https://doi.org/10.1016/j.psep.2023.06.006.
[38] V. Molkov, D. Makarov, E. Prost, On numerical simulation of liquefied and gaseous hydrogen releases at large scales, in: International Conference on Hydrogen Safety, 2005.
[39] S.R. Hanna, R.E. Britter, Wind Flow and Vapor Cloud Dispersion at Industrial and Urban Sites, Center for Chemical Process Safety of the, American Institute of Chemical Engineers., 2002.
[40] H. Ebne-Abbasi, D. Makarov, V. Molkov, CFD model of refuelling through the entire equipment of a hydrogen refuelling station, Int. J. Hydrog. Energy 53 (2024) 200–207, https://doi.org/10.1016/j.ijhydene.2023.12.056.
[41] I. Simonovski, D. Baraldi, D. Melideo, B. Acosta-Iborra, Thermal simulations of a hydrogen storage tank during fast filling, Int. J. Hydrog. Energy 40 (2015) 12560–12571, https://doi.org/10.1016/j.ijhydene.2015.06.114.
[42] J.M. Smith, H.C. Van Ness, M.M. Abbott, M.T. Swihart, Introduction to Chemical Engineering Thermodynamics, Eighth, McGraw Hill Education, 2018.
[43] D. Baraldi, D. Melideo, A. Kotchourko, K. Ren, J. Yanez, O. Jedicke, S.G. Giannissi, I.C. Tolias, A.G. Venetsanos, J. Keenan, D. Makarov, V. Molkov, S. Slater, F. Verbecke, A. Duclos, Development of a model evaluation protocol for CFD analysis of hydrogen safety issues the SUSANA project, Int. J. Hydrog. Energy 42 (2017) 7633–7643, https://doi.org/10.1016/j.ijhydene.2016.05.212.
[44] S. Mohanty, S. Brennan, V. Molkov, CFD modelling of methane dispersion from buried pipeline leaks: experimental validation and hazard distance estimation, Process Saf. Environ. Protect. 187 (2024) 1540–1557, https://doi.org/10.1016/j.psep.2024.05.078.
[45] SUSANA Project Team, Report on verification and validation procedures. [online] SUSANA Project Deliverable D4.2. Available at: <https://www.h2fc-net.eu/collaboration/susana-database/susana-public-documents/>, (2016).
[46] S.W. Kieffer, Sound speed in liquid-gas mixtures: water-air and water-steam, J. Geophys. Res. 82 (1977) 2895–2904, https://doi.org/10.1029/JB082i020p02895.
[47] I.S. Radovskii, Speed of sound in two-phase vapor-liquid systems, J. Appl. Mech. Techn. Phys. 11 (1973) 778–784, https://doi.org/10.1007/BF00851905.
[48] E.E. Michaelides, K.L. Zissis, Velocity of sound in two-phase mixtures, Int. J. Heat. Fluid. Flow. 4 (1983) 79–84, https://doi.org/10.1016/0142-727X(83)90006-1.
[49] D.J. Picard, P.R. Bishnoi, Calculation of the thermodynamic sound velocity in two-phase multicomponent fluids, Int. J. Multiph. Flow 13 (1987) 295–308, https://doi.org/10.1016/0301-9322(87)90050-4.
[50] T. Kawai, An interpretation of sound velocity in two phase mixtures, J. Nucl. Sci. Technol. 7 (1970) 317–320, https://doi.org/10.1080/18811248.1970.9734691.